Copyright

by

William Fassett Hickey

2011

The Thesis Committee for William Fassett Hickey
Certifies that this is the approved version of the following thesis:

An Investigation into the Failure of Aluminum Alloys

APPROVED BY
SUPERVISING COMMITTEE:

Supervisor:

K. Ravi-Chandar

Chad Landis

An Investigation into the Failure of Aluminum Alloys

by

William Fassett Hickey, B.S.

Thesis

Presented to the Faculty of the Graduate School of

The University of Texas at Austin

in Partial Fulfillment

of the Requirements

for the Degree of

Master of Science in Engineering

The University of Texas at Austin

August 2011

Dedication

To my wife Cathleen Ray Hickey.

Acknowledgements

I would like to thank my advisor Dr. K Ravi-Chandar for allowing me this opportunity to further my education at the University of Texas at Austin. I would also like to thank Ali Ghahremaninezhad for his assistance in conducting many experiments. Thanks to machinists Rick Maldanado, Travis Crooks and Ricardo Palacious for their contributions to this project.

Abstract

An Investigation into the Failure of Aluminum Alloys

William Fassett Hickey, M.S.E.

The University of Texas at Austin, 2011

Supervisor: K. Ravi-Chandar

The rate dependence of several aluminum alloys (6061, 7075, 5083) was examined through the means of quasi-static tension tests, dynamic tension tests, and split pressure Hopkinson bar tests. The macroscopic strains of the quasi-static and dynamic tension tests were measured after failure within the uniform region and the necked region using high-resolution images and edge detection.

The study continued with an exploration into the plane-stress ductile fracture of Al 6061 in the T6 and O condition. Digital image correlation (DIC) was used to find the displacement and strain fields, and a numerical method for calculating the stress fields for a power law hardening material was developed. The J-integral was then calculated locally. The effect of strain hardening on the type of fracture (slant or flat) was also investigated. Macroscopic and microscopic observations of the fracture were made with DIC and by dissecting, polishing and/or etching the broken fracture specimens. Local failure strain measurements were made on the grain level and compared with those found through traditional failure strain measurements.

Table of Contents

List of Tables

List of Figures

Chapter 1: Introduction

1.1 Project Background

Aluminum alloys are one of the most consumed structural materials in the world, and they are used in a vast number of applications due to their favorable properties (Kaufman 2000). Some aluminum alloys are well suited for marine applications because of their corrosion resistance, while others have high fracture toughness desirable for fracture critical operations.

The 6000-series aluminum alloys have many favorable features: heat treatability, weldability, extrudability and corrosion resistance. The 6000-series alloys are great structural elements because they can be extruded and worked into any shape in the annealed state and strengthened through simple heat treatments.

The 5000-series alloys are widely used in marine applications due to their superior corrosion resistance. Other beneficial characteristics include high fracture toughness and notable weldabitlity. Aluminum 5083 is more widely used than other 5000-series alloys due to its higher strength.

The 7000-series aluminum alloys are the highest strength aluminum alloys and have been widely used in aircraft structures due to high fracture toughness.

The present interest is in properly characterizing a particular set of aluminum alloys for simulation of the implosion of cylindrical aluminum tubes at high pressures, such as those experienced at deep-water depths. When the buckling and implosion of a tube occurs, the material undergoes significant plastic deformation, and the internal

structure fractures at multiple locations. Proper characterization of the material and the underlying fracture processes are important building blocks in understanding this complex process. The alloys of interest are Al 6061-T6, Al 5083-H116 and Al 7075-T73.

1.2 Outline of Present Study

This study began with a series of tension tests on three different aluminum alloys: Al 7075, Al 5083 and Al 6061. First, each alloy underwent uniaxial quasi-static loading to understand the basic material behavior and isotropic plasticity. Furthermore, the rate dependent behavior of these alloys was examined by employing the dynamic drop tower for strain rates on the order of 10^2 strain/sec. Digital image correlation was used to record the strain for both the quasi-static and dynamic drop tower tension tests. Successful split pressure Hopkinson bar compression tests for strain rates on the order of 10^3 strain/sec were also performed.

The macroscopic failure strains under quasi-static and dynamic tensile loading conditions were measured in the uniform region and within the necked region. Data is provided for all three alloys.

The report continues with an exploration into the ductile fracture of Al 6061-T6 and Al 6061-O using single edge notched tension specimens. Digital image correlation was used to find the displacement and strain fields, and a novel numerical method for calculating the stress fields for a power law hardening material was developed. After calculating the stress field, the J-integral was calculated using both the line integral and

the area integral formulations. In order to establish a failure criterion, the J-integral at crack initiation was documented.

Finally, this report concludes with a brief study on the macroscopic and microscopic fracture observations in both the T6 and O materials. Qualitative observations are made for the plastic zone shapes of experimental DIC data. The fracture surfaces are examined using a scanning electron microscope, and different specimens are sectioned for internal views at different orientations and etched for grain level strain measurements. These strain measurements are compared with the macroscopic failure strains found from the tension tests.

Chapter 2: Material Behavior

Three aluminum alloys- Al 6061-O & T6, Al 5083-H116 and Al 7075-T73- were chosen for this study. Each alloy employs different alloying agents, heat treatments and/or cold working treatments for strengthening.

Aluminum 6061 is a 6000-series aluminum that contains silicon and magnesium as the primary alloying agents. The material is investigated in two forms, the T6 condition and the O annealed condition. In the T6 condition, the material is solution heat treated and then artificially aged: an artificially aged material undergoes aging at high temperatures whereas natural aging occurs at room temperature. In the solution heat treatment stage, the material is heated, and all alloying agents are in solution. The material is quenched, and this supersaturated solution contains a single phase. The material is then reheated to a desired temperature where diffusion is favorable, and precipitates and intermediate phases start to grow and nucleate. At first, the precipitates are small particles evenly dispersed throughout the matrix, but as time passes these precipitates start to nucleate and become larger. The size and spacing of the precipitates is dependent upon how long the material is held at the aging temperature. Exhaustive studies on the effect of aging times on precipitate size and grain size have been performed and well documented (see Handbook of Aluminum by Totten and MacKenzie, 2003). Precipitation hardening is an effective hardening mechanism because it inhibits the movement of dislocations during plastic deformation and thus raises the material strength. The Al 6061-T6 has a high yield strength (43,000 psi) but does not exhibit significant strain hardening.

The O in Al 6061-O denotes the annealed condition. In the annealing process, the material is heated above the re-crystallization temperature, held there for a period of time and slowly cooled. During this process, the alloy returns to thermodynamic equilibrium. Annealing reduces the yield strength but increases the ductility. The 6061 alloy was received in the T6 condition and annealed in house using a heat treating furnace. To anneal the Al 6061-T6, the specimens are heated to a temperature of 760° F and held for 2-3 hours, then cooled in the furnace at a rate of 50° F per hour until 500° F and finally air cooled to room temperature.

Aluminum 5083-H116 is a 5000-series aluminum that uses magnesium as the primary alloying agent. The H116 denotes that it is cold worked and heat treated, and this combination of heat treatment and cold working make it especially resistant to corrosion in harsh environments.

Aluminum 7075 is a 7000-series aluminum that uses zinc, magnesium and copper as the primary alloying agents. This material was received and tested in the T73 condition, which designates an over-aged precipitate-hardened material without strain hardening. To achieve the T73 condition, the 7075 alloy first undergoes solution heat treatment; then it is artificially aged past the maximum strength. The amount of aging changes the material strength. At first, the strength increases with aging time, and then it reaches a maximum and starts to decrease. Over-aged materials are aged past the peak strength, and this sacrifice in material strength though over aging brings about other desirable properties, such as stress corrosion cracking resistance and increased fracture toughness.

2.1 DIGITAL IMAGE CORRELATION

Digital Image Correlation (DIC) was used throughout this investigation to determine the surface displacements and strains. This method was developed in the early 1980s specifically for use in experimental measurement of strain; the following introduction to DIC follows from the presentation of Sutton et al., (1985).

A small line segment PQ in a continuum with dimensions (dx, dy, dz) undergoes deformation to become P^*Q^* with dimensions (dx^*, dy^*, dz^*). The point P is located at (x, y, z), and Q is located at $(x + dx, y + dy, z + dz)$. The deformed points P^* and Q^* can be written in terms of the original coordinates and the components of displacement, (u, v, w).

$$\begin{aligned} P^* &= (x^*, y^*, z^*) = [x + u(P), y + v(P), z + w(P)] \\ Q^* &= (x^* + dx^*, y^* + dy^*, z^* + dz^*) \end{aligned} \tag{2.1}$$

From Eqs.(2.1), the dimensions of the displaced line P^*Q^* can be written in terms of (u, v, w).

$$\begin{aligned} dx^* &= u(Q) - u(P) + dx \\ dy^* &= v(Q) - v(P) + dy \\ dz^* &= w(Q) - w(P) + dz \end{aligned} \tag{2.2}$$

After a Taylor series expansion of the displacement functions in Eqs. (2.2), the components of the displaced line can be rewritten in terms of the displacement gradients and the original line dimensions.

$$dx^* = \left(1 + \frac{\partial u}{\partial x}\right) dx + \frac{\partial u}{\partial y} dy + \frac{\partial u}{\partial z} dz$$

$$dy^* = \frac{\partial v}{\partial x} dx + \left(1 + \frac{\partial v}{\partial y}\right) dy + \frac{\partial v}{\partial z} dz \tag{2.3}$$

$$dz^* = \frac{\partial w}{\partial x} dx + \frac{\partial w}{\partial y} dy + \left(1 + \frac{\partial w}{\partial z}\right) dz$$

In the case of 2-dimensional deformation, the surface of an illuminated object has a certain intensity associated with each pixel in the domain. In the undeformed state, a subset of pixels centered at P has a unique intensity.

$$f(P) = f(x, y) \tag{2.4}$$

If the subset if deformed, the center of the subset moves to P^*.

$$f^*(P^*) = f^*[x + u(P), y + v(P)] \tag{2.5}$$

If another point Q within the subset is defined at location $(x + dx, y + dy)$, this point also has a unique intensity.

$$f(Q) = f(x + dx, y + dy) \tag{2.6}$$

Similarly, after deformation the point Q moves to point Q^*.

$$f^*(Q^*) = f^*(x + u(Q) + dx, y + v(Q) + dy) \tag{2.7}$$

The primary assumption of DIC is that the subset undergoes deformation, but the intensity value of the subset is not changed from the deformation, i.e. $f(Q) = f(Q^*)$.

$$\begin{aligned} f(P) &= f[x + u(P), y + v(P)] \\ f(Q) &= f[x + u(Q) + dx, y + v(Q) + dy] \end{aligned} \tag{2.8}$$

In order to use Eqs. (2.3), straight lines are assumed to remain straight after deformation because of their infinitesimal dimensions. Therefore, the subset of pixels needs to be

small relative to other length scales in the problem such as width and thickness or the lengths over which large strain gradients occur. Next, Eqs. (2.8) must be combined with Eqs. (2.3).

$$\begin{aligned} f^*[P^*] \\ = f\Big[x + u(P) + \frac{\partial u}{\partial x}(P)dx + \frac{\partial u}{\partial y}(P)dy + dx, y + v(P) + \frac{\partial v}{\partial x}(P)dx \\ + \frac{\partial v}{\partial y}(P)dy + dy\Big] \end{aligned} \tag{2.9}$$

In Eq. (2.9), the six unknown displacement derivatives (strains) are determined by comparing the original subset intensity and location with the deformed subset intensity and location. All six unknowns can be determined throughout the domain by an iterative procedure designed to maximize or minimize the cross-correlation coefficient.

$$C\left(u, v, \frac{\partial u}{\partial x}, \frac{\partial u}{\partial y}, \frac{\partial v}{\partial x}, \frac{\partial v}{\partial y}\right) = \frac{\int_{\Delta M^*} f(x,y) f^*(x+\xi, y+\eta) dA}{\left\{\int_{\Delta M}[f(x,y)]^2 dA \int_{\Delta M^*}[f^*(x+\xi, y+\eta)]^2 dA\right\}^2} \tag{2.10}$$

The quantities ΔM and ΔM^* denote the subset in the undeformed image and deformed image, respectively.

$$\begin{aligned} \xi &= u + \frac{\partial u}{\partial x}\Delta x + \frac{\partial u}{\partial y}\Delta y \\ \eta &= v + \frac{\partial v}{\partial x}\Delta x + \frac{\partial v}{\partial y}\Delta y \end{aligned} \tag{2.11}$$

In this iterative procedure, a computer algorithm searches for values of the unknown quantities that maximize the cross-correlation coefficient. For our tests, the Aramis DIC software is used to implement this procedure.

The Aramis DIC system consists of 2 high-resolution cameras (1280 x 1024 pixels, 12bit digital), a tripod stand for the cameras, computer hardware and software. This system is capable of calculating both 2-dimensional and 3-dimensional strains, but for this study, only 2-dimensional calculations were needed.

DIC is very simple to implement, and one of the most attractive features of DIC is that the non-contact nature of the measurement system. The specimen simply needs to be covered with a stochastic pattern to provide a variation in the surface intensity of the specimen in order to facilitate the correlation. For our test specimens, the variation in intensity was accomplished by spraying the specimen surface first with white spray paint and then with a light layer of black spray paint. This stochastic pattern provided the perfect variation in light intensity for use with the Aramis DIC software.

The Aramis DIC system software can be used along with the hardware to capture images. The user can specify the rate of image acquisition, and the images are automatically recorded and loaded into the software. The image acquisition system has a minimum acquisition rate of one image per second and a maximum of about 10 images per second. Images can also be collected from other camera systems, such as high-speed cameras, and input into the system. The same analysis is performed on images from other sources.

After the experiment is completed and all images have been recorded or loaded, the software analyzes them for strain and displacement. The user must choose the step size and facet size for the calculations. The facet size is the size of the subset, and the step size is the number of pixels skipped in between the center points of neighboring subsets.

The larger the facet sizes the better the accuracy, but the smaller the facet sizes the better the resolution. The smaller step size provides better resolution, but significantly increases the amount of time necessary to perform the computations.

Upon successful analysis of all images, the results are output in a text file for each image or stage. The output text files include the 2-dimensional strains and displacements, the fixed reference frame coordinates and the deformed reference frame coordinates.

2.2 TENSION AND COMPRESSION TESTS

Characterization of these three aluminum alloys began with quasi-static tension tests, followed by dynamic drop tower tension tests, and then split Hopkinson pressure bar tests. The aluminum alloys were received from the manufacturer in large sheets, 60 inches by 72 inches and machined into various types of specimens. The Al 6061-T6 sheets had a thickness of 0.096 inches, and the Al 5083-H116 and Al 7075-T73 sheets had thicknesses of 0.125 inches.

2.2.1 Quasi-Static Tension Tests

Quasi-static tension test specimens were created from the sheet stock using wire electrical discharge machining (EDM). Specimen dimensions can be seen in Figure 2.1. The tension test specimens were created parallel and perpendicular to the rolling direction, denoted by W and A respectively. For example, the test Al 6061-T6-W stands for a quasi-static tension test of alloy Al 6061-T6 cut parallel to the rolling direction. Testing specimens in the different rolling directions will allow us to examine material anisotropy.

All quasi-static tension tests were performed on an Instron 4482 testing machine in displacement control at a crosshead displacement rate of 0.01 inches per minute; this corresponds to a strain rate of about 0.001 s^{-1}. The load and crosshead displacement were recorded using the Instron Series IX data acquisition software. The Aramis DIC system collected one image per second for the duration of the test. After completion of the experiment, the images were analyzed for displacement and strain using the Aramis software.

After experimentation, the quasi-static tests were fit with a Ramberg-Osgood power law.

$$\varepsilon = \frac{\sigma}{E}\left[1 + \alpha\left(\frac{\sigma}{\sigma_y}\right)^{n-1}\right] \tag{2.12}$$

The parameters calibrated for each alloy are presented in Table 2.1.

2.1.2 Dynamic Tension Tests

The dynamic tension tests allow for tensile stain rates on the order of 10^2 s^{-1}. The dynamic drop tower test frame is shown in Figures 2.2 and 2.3, and the specimen dimensions are shown in Figure 2.4. The dropper was lifted along a rail to a height of approximately 2 meters and held in place by an electromagnet. After the high-speed digital camera and load sensor were properly set-up, the voltage to the electromagnet was decreased causing the dropper to be released and fall. All load measurements were made using a PCB 226C ICP quartz force sensor. The tensile load capacity of the force sensor is 20,000 pounds. The force sensor output was in voltage, and the calibration factor was -

0.1058 millivolts per pound (negative signal in tension). During the drop tests, a digital oscilloscope was used to measure the force signal from the sensor at a sampling rate of 2.5 G samples/s. The oscilloscope recorded the signal when it was triggered by the decrease in voltage from the change in sensor voltage.

Images of the dynamic tension tests were recorded using a Photron Fastcam SA1 digital high speed camera. This digital camera is capable of recording images at a full resolution of 1012 by 1012 pixels at a rate of 2000 frames per second, but as the recording frequency is increased, the resolution of the recorded images decreases. For the dynamic drop tests, the camera recorded at 40,000 frames per second at a resolution of 384 by 320 pixels. A light sensor was used to trigger the high-speed camera to record digital images of the test. After the dropper was released, the dropper interrupted the rays of light entering the light sensor, and the light sensor output a TTL signal that triggered the camera.

The dynamic tension test images were analyzed for displacement and strain using the Aramis DIC software, and the stress was calculated from the force sensor data. Determining the end points for each test synchronized the stress and strain data. The force data had a sharp decline when the specimen broke, and the last image of a fully intact tension specimen was the end point used for the strain data. The two endpoints were used to align the data in time, and the two data sets were interpolated to create a stress-strain curve.

The force sensor signals were noisy and included a resonance frequency from the specimen and test structure. In order to remove these high frequencies, the *butter* and

filtfilt functions were utilized in a MATLAB routine. The *butter* function creates a Butterworth filter, which was chosen for this specific application because the magnitude response of the Butterworth filter is "maximally flat in the passband and monotonic overall." First, the filter had to be created by inputting the order of the filter, the normalized frequency and the type of filter. For these tests, a third order, low pass Butterworth filter with cutoff frequencies between 1000 and 2,200 Hertz was created and applied to the signal using the *filtfilt* function. This function filters the data in both the forward and reverse directions for a zero phase shift, which is particularly useful since the data is being interpolated in time to create stress-strain curves. A sample of unfiltered and filtered force sensor data is shown in Figure 2.5. A sample stress-strain curve obtained from filtering the load data, computing the strains, and interpolating in time is compared with a quasi-static tension test in Figure 2.6. Here the two curves fall onto one another and confirm the capability of the test method to yield the dynamic stress-strain curve.

2.1.3 Split Hopkinson Pressure Bar Tests

In order to examine the material behavior at even higher strain rates not achieved through the drop tower, a split Hopkinson pressure bar was used to reach strain rates of approximately 10^3 strain/sec. But, we note that the quasi-static and drop tower tests were in tension whereas the Hopkinson bar tests are in compression.

The split Hopkinson pressure bar consists of a firing chamber, a projectile and two bars. The two bars and projectile are typically made from high strength maraging

steel. The firing chamber uses compressed air to launch the projectile. The two bars are aligned longitudinally, and a specimen is placed between them as illustrated in Figure 2.7. The air chamber is filled with compressed air, and when the air is released, the projectile rapidly ejects the chamber and strikes the input bar. A compressive strain wave travels through the input bar, specimen and output bar. Part of the compressive wave is reflected as a tensile wave at the input bar-specimen interface while the other part of the compressive wave travels through the specimen and through the output bar. The different waves are recorded in the input and output bars by longitudinally arranged strain gages. The stress and strains are calculated from the recorded strain gage signals using standard methods of analysis of Hopkinson pressure bar. Integrating the reflected wave with time and multiplying by constants of the test set-up provides the strain in the specimen:

$$\varepsilon(t) = \int \frac{2c}{l_o} \varepsilon_R(t) dt \tag{2.13}$$

The parameter c is the elastic wave speed in the input and output bar and is found by taking the square root of the elastic modulus divided by the density, and l_o is the initial specimen length. The engineering stress is calculated simply by multiplying the transmitted strain signal with the constants of the test set-up.

$$\sigma(t) = E_b \left(\frac{A_b}{A_s}\right) \varepsilon_t(t) \tag{2.14}$$

Here, A_b and A_s are the cross sectional areas of the input/output bars and specimen, respectively, and E_b is the elastic modulus of the input/output bars. The stress and strain from Eq. (2.13) and Eq. (2.14) were interpolated in time to create a stress-strain curve.

The specimens used for this test were small tabs with a diameter of 5 mm and a thickness of the sheet material, either 0.096" or 0.125". A sample calculation of the stress-strain curve obtained from the SHPB is shown in Figure 2.8, superposed on the quasi-static stress-strain curve.

2.2 Determination of Strain from Post-Mortem Image Processing

There exists no definitive definition of failure strain. For our purposes, the quasi-static failure strain was defined as the average strain within the localization at failure of specimen. This value of strain was found in conjunction with the uniform strain in the specimen at failure, this is the strain measured at one specimen width from the localization region. To find the failure strain, the material is assumed to be incompressible:

$$A_o l_o = Al \tag{2.15}$$

Where $(A_o\ l_o)$ and $(A\ l)$ are the cross sectional area and length of the specimen before and at any stage of deformation, respectively. The longitudinal strain was calculated by rearranging Eq. (2.15) and taking the natural log of both sides.

$$\varepsilon = ln\frac{l}{l_o} = ln\frac{A_o}{A} \tag{2.16}$$

In order to determine the local strain at failure, initially the width and thickness of the broken specimens were measured using a caliper, but the measurements were not precise enough for this calculation. The deformation gradient of the thickness and the width was too large to be precisely measured by the relatively large caliper measuring length.

Therefore, an edge detection algorithm was created using MATLAB, and high-resolution digital images were taken with a Nikon D90 digital camera. The digital sensor of the camera is used to record images with a resolution of 12.3 million pixels. This simple routine could detect the edges of the broken specimen to within 3 to 5 pixels. A calibration image of a high-resolution ruler was captured for each set of images. The values of width and thickness were recorded, and the strain was calculated.

A sample image of the output from the edge detection routine is shown in Figure 2.9. This is for the thickness direction, and one must also rotate the specimen and record the corresponding width direction. To find the necessary thickness values, one would record the thickness one width away from the center of the localization and then the thickness within the localization. This measurement was combined with similar measurements from the width direction and the strain was calculated as shown in Eq. (2.16).

The failure strain and the uniform strain at failure are presented in Table 2.2 alongside the standard deviations for each group of tests. The results are also presented graphically in Figures 2.10-13.

2.3 Experimental Results and Master Plots

The uniform and failure strains of all alloys are compared in Figure 2.10. The epsilon ε in these plots signifies the strain, whereas the superscript denotes the type of test (quasi-static qs or dynamic d) and the subscript denoted the strain measurement (uniform u or failure f). The uniform strain is the found one width from the localization,

and the failure strain is measured within the localization. The Al 6061 material is the most ductile and experiences the highest strains. The Al 5083 experiences the largest disparity in the failure strain between the quasi-static and dynamic tests. The uniform and failure strains of the Al 7075 exhibit small increases between the quasi-static and dynamic loadings.

Furthermore, in Figures 2.11-13 the comparison in the uniform and failure strains tested in different grain orientations are compared for each alloy. The Al 6061 material has negligible effect of strain rate on the uniform strain; however, the failure strains are noticeably lower when tested across the grain. The Al 5083 undergoes no noticeable difference in either strain for the different loading directions. The Al 7075 experiences negligible change in the uniform strain, but the failure strains are much lower for the across the grain material.

Additionally, plots containing the stress-strain curves at different strain rates along with the uniform and failure strains with respective standard deviations are presented in the master plots in Figure 2.14 through Figure 2.20. The master plots allow all the data from the previously described experiments to be presented in a concise manner.

The master plots for Al 6061-T6 in W and A directions are presented in Figures 2.14-15. Similar trends are observed for both rolling directions. No observable rate dependence for the W material, and very small rate dependence observed in the dynamic tension test for the A material. The uniform and failure strains both experience moderate increases with strain-rate.

In Figure 2.16, the quasi-static stress curve for the Al 6061-O material is fitted with the Ramberg-Osgood fit. The uniform and failure strains of this material are much higher than the T6 condition. This material experiences uniform stains around 20% whereas the failure strain is approximately 75%.

The master plots for Al 5053-H116 are shown in Figures 2.17-18. For both rolling directions, the material exhibits no rate dependence in the stress-strain response; however, the dynamic failure strain of the Al 5083-H116 is nearly three times the quasi-static value, and uniform dynamic strain at failure is almost double the quasi-static result. This signifies a large increase in ductility with strain rate, but the absence of strain rate dependence in the stress-strain response suggests that the ductility increase can be attributed to inertial effects.

In Figures 2.19-20, the master plots for Al 7075-T73 are presented for W and A rolling directions. This is the only material that experiences strain-rate dependence in the stress-strain behavior of the material. The uniform stains in the W and A directions both experience small increases, while the failure strains in the W direction experience negligible increase and in the A direction experience a larger increase.

Overall, these particular materials do no exhibit significant strain-rate dependence for the strain rates tested (up to 10^3 s^{-1}). The strains-to-failure measured within the localization region are quite large; however, they exhibit significant scatter, especially when compared to the scatter of the uniform strains at failure. The large increase in failure strains from the quasi-static to dynamic tension tests without a change in the stress-strain behavior of the material can be attributed to inertial effects.

The failure strains measured from the edge-detection routine are "average" strains. For a more exact measurement, the strain can be measured on the grain level of the material. These strains are much larger than the average measure. This will be discussed in more detail in Chapter 4.

Table 2.1: Ramberg-Osgood parameters

Material	E **(psi)**	σ_y **(psi)**	n	α
Al 6061-T6	1E7	43,000	17.03	0.4537
Al 6061-O	1E7	6,500	4.277	1.126
Al 5083-H116	1E7	36,160	7.108	0.882
Al 7075-T73	1E7	54,500	9.92	0.445

Table 2.2: Macroscopic uniform and failure strains with standard deviation

Group	$\bar{\varepsilon}_f$	**σ**	$\bar{\varepsilon}_u$	**σ**
Al 6061-O-W	0.7458	-	0.2183	-
Al 6061-O-A	0.7027	-	0.2183	-
Al 6061-T6-W	0.5135	0.08842	0.04942	0.01290
DT 6061-T6-W	0.6483	0.02947	0.1421	0.008663
Al 6061-T6-A	0.3918	0.02796	0.06725	0.005240
DT 6061-T6-A	0.5896	0.05158	0.1253	0.02223
Al 5083-H116-W	0.1981	0.03228	0.1031	0.02446
DT 5083-H116-W	0.6056	0.01576	0.1944	0.08813
Al 5083-H116-A	0.2318	0.01411	0.1138	0.01168
DT 5083-H116-A	0.6040	0.03992	0.1655	0.01955
Al 7075-T73-W	0.3810	0.04080	0.07251	0.007620
DT 7075-T73-W	0.3858	0.04515	0.1157	0.007425
Al 7075-T73-A	0.2810	0.04346	0.07148	0.007926
DT 7075-T73-A	0.3305	0.02250	0.1131	0.03272

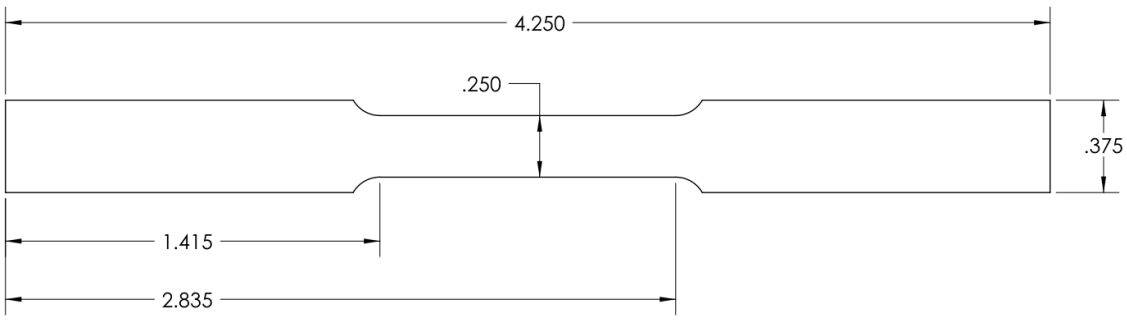

Figure 2.1: Quasi-static tension specimen

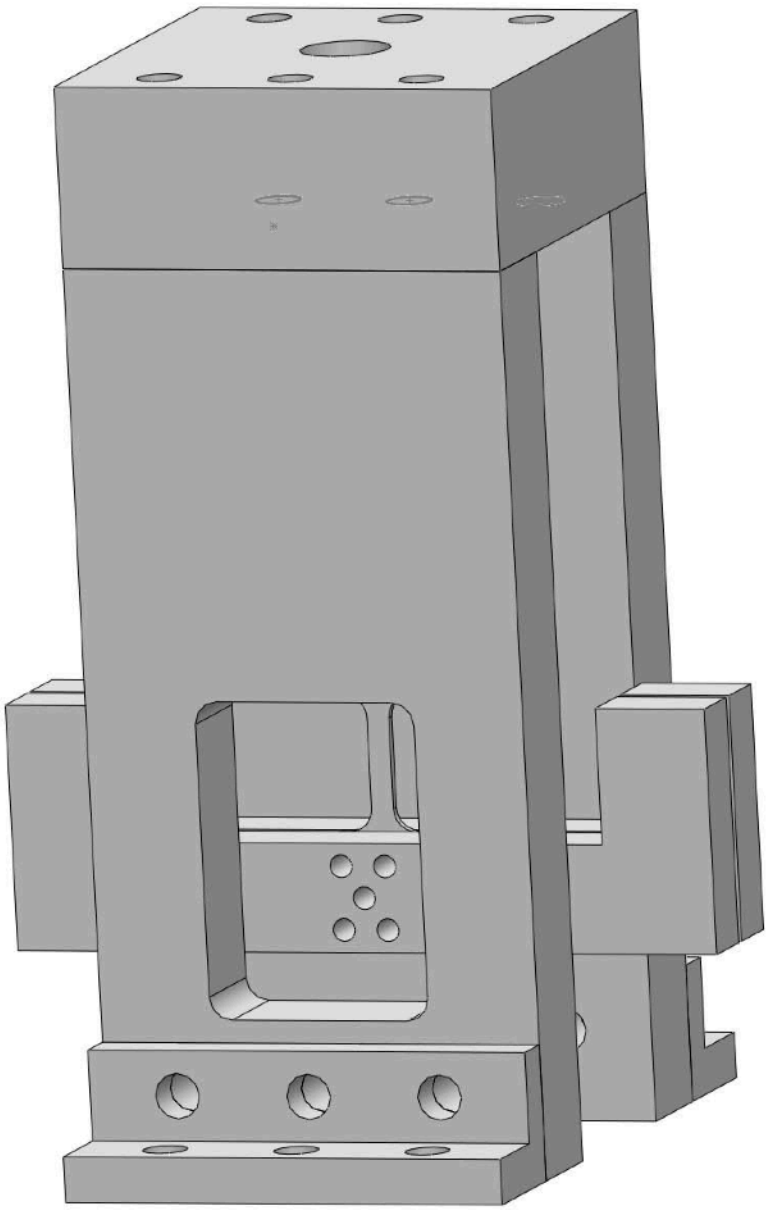

Figure 2.2: Dynamic tension test fixture

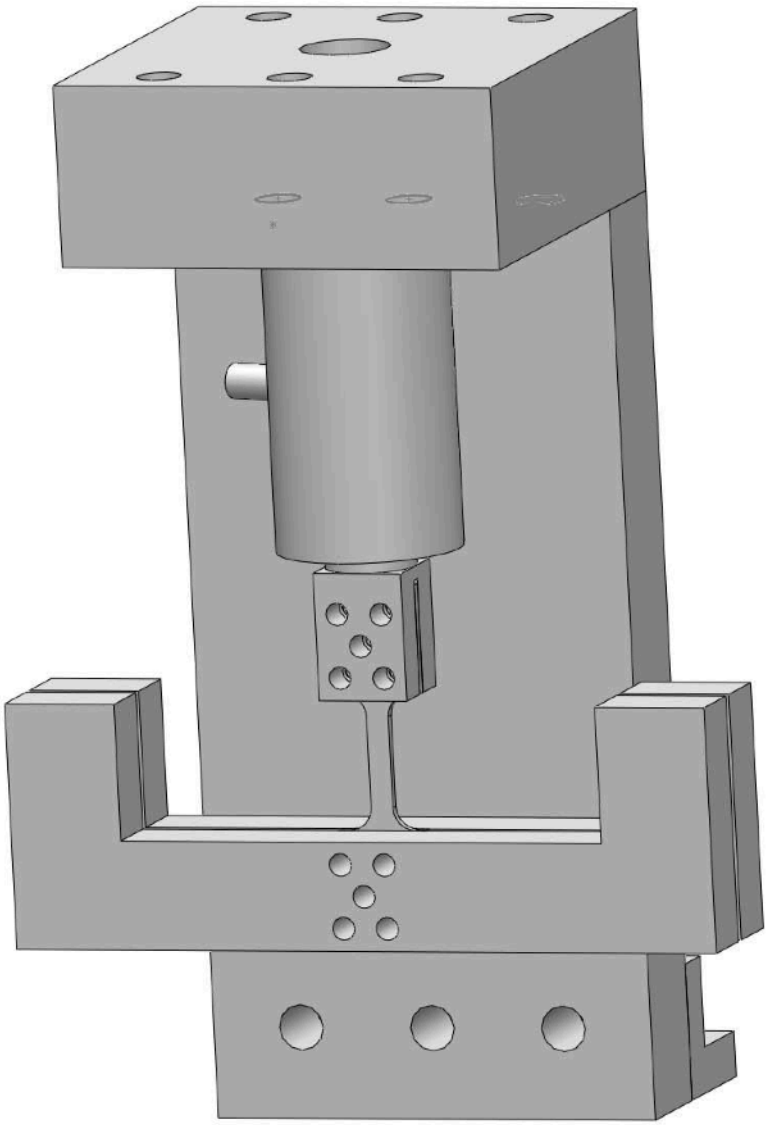

Figure 2.3: Dynamic tension test frame with front plate removed

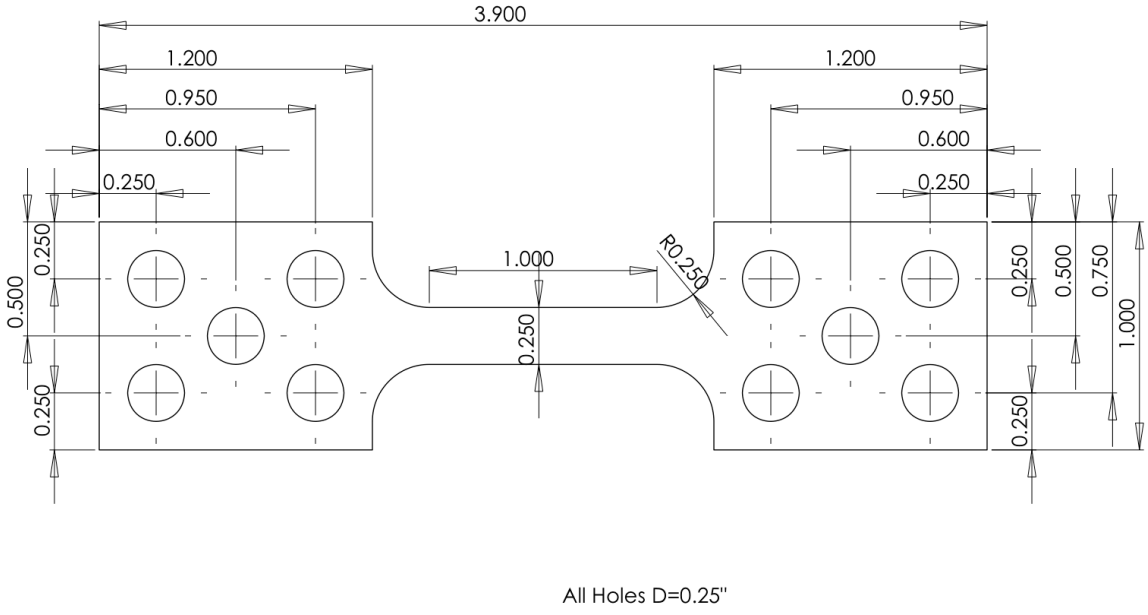

Figure 2.4: Dynamic tension test specimen

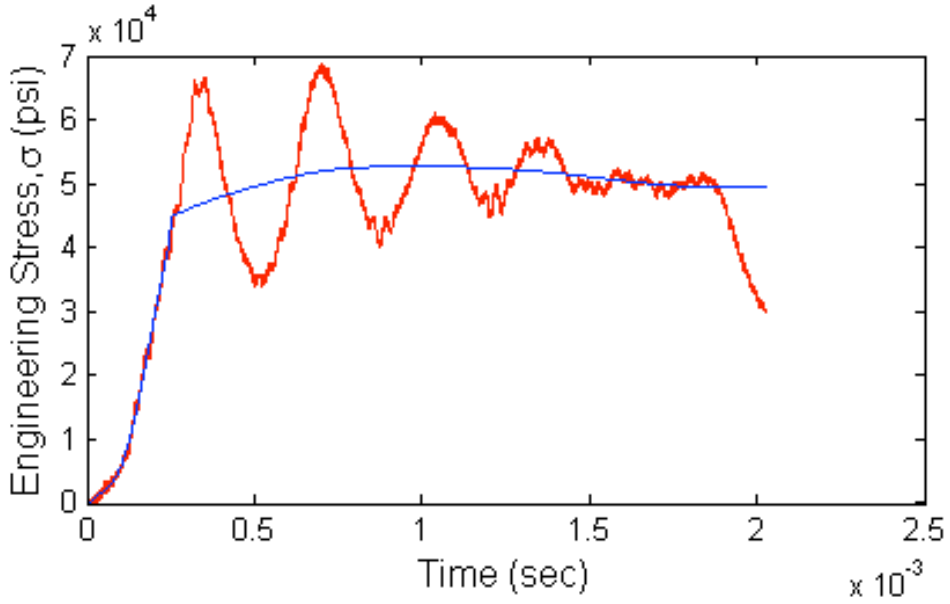

Figure 2.5: Filtered and unfiltered data from dynamic tension test of Al 5083-H116

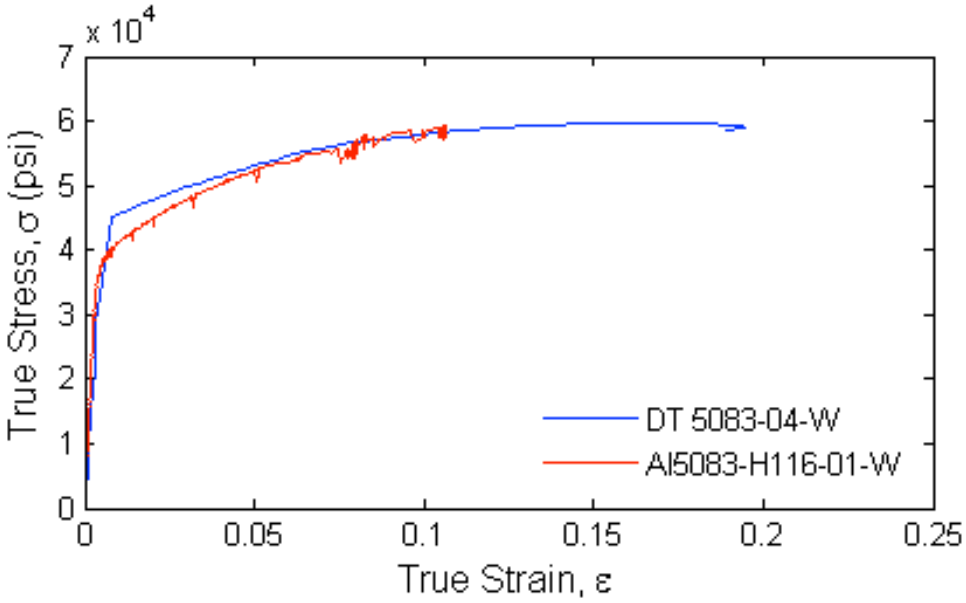

Figure 2.6: Comparison of quasi-static (Al5083-H116-01-W) and dynamic (DT5083-04-W) stress-strain curves

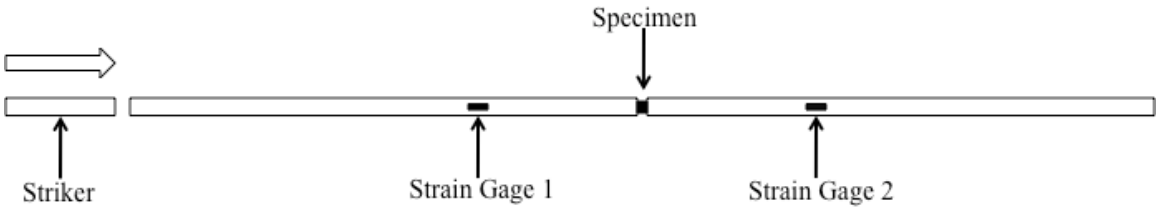

Figure 2.7: Split Hopkinson pressure bar

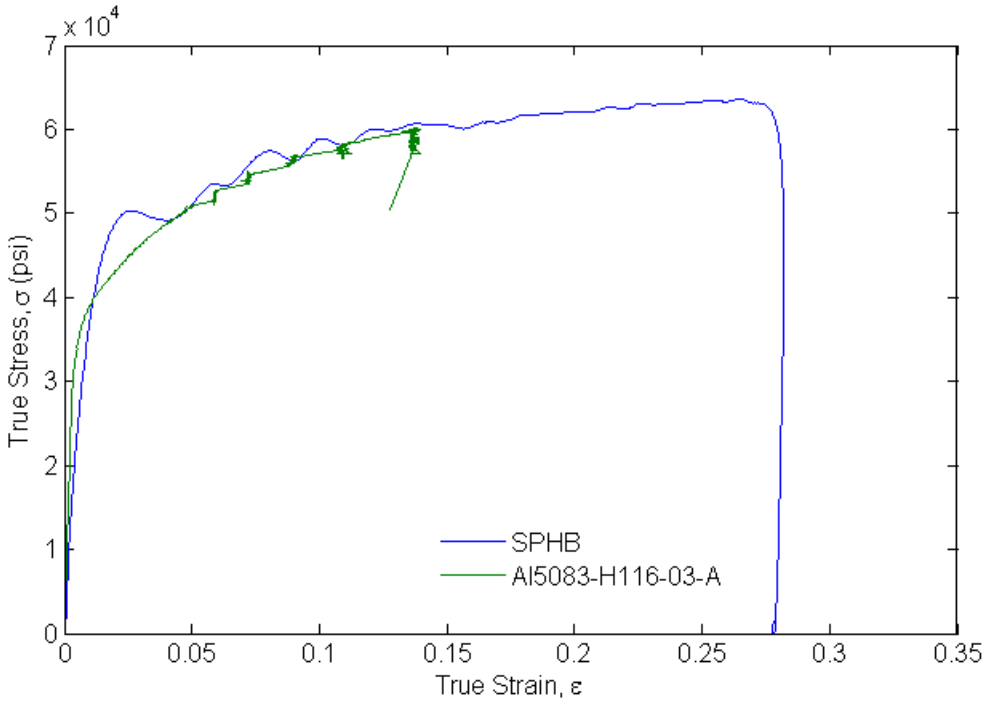

Figure 2.8: Comparison of quasi-static tension test (Al5083-H116-01-W) and split Hopkinson pressure bar test for Al 5083-H116

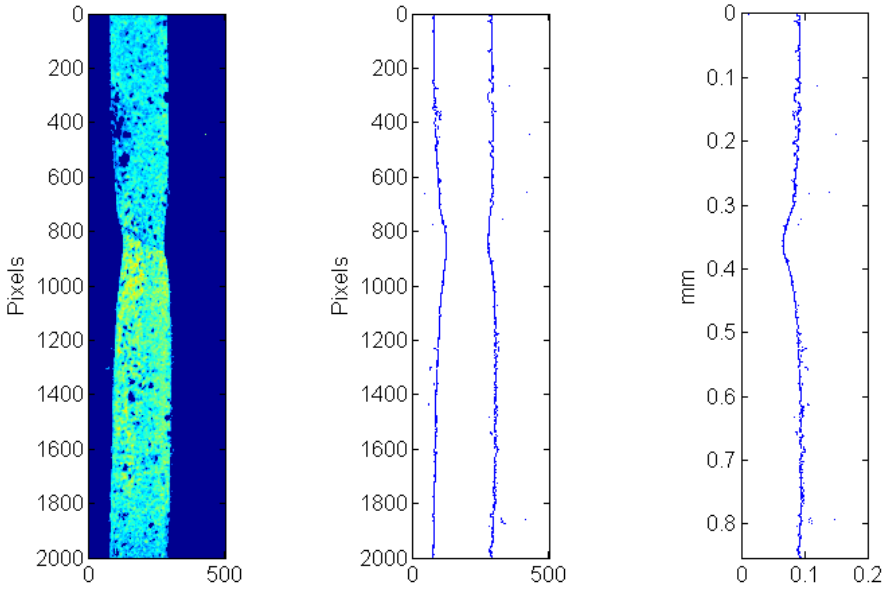

Figure 2.9: Example of edge detection routine used to find uniform and failure strains

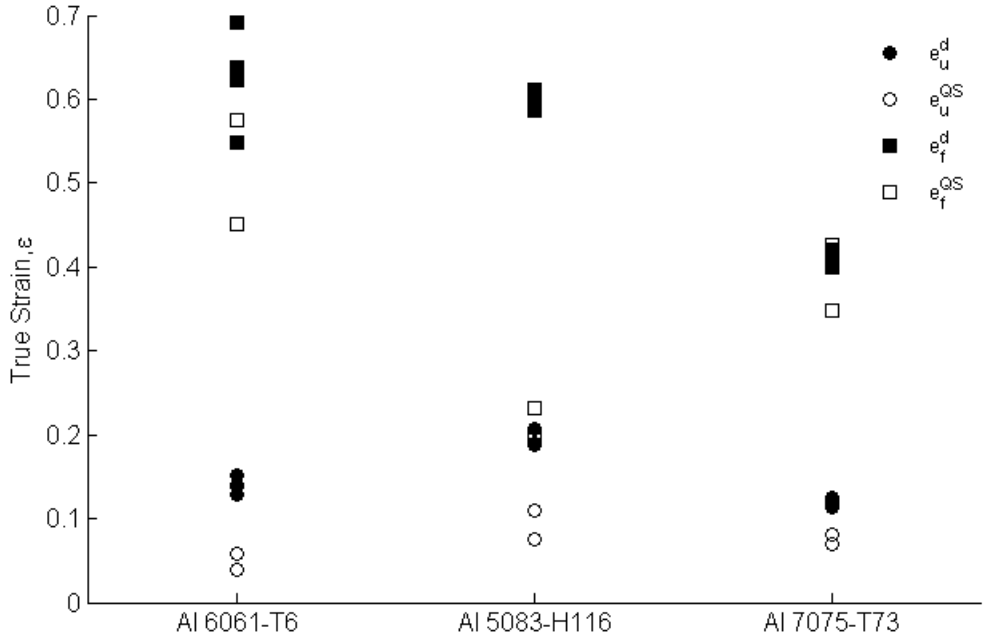

Figure 2.10: Comparison of uniform and failure strains

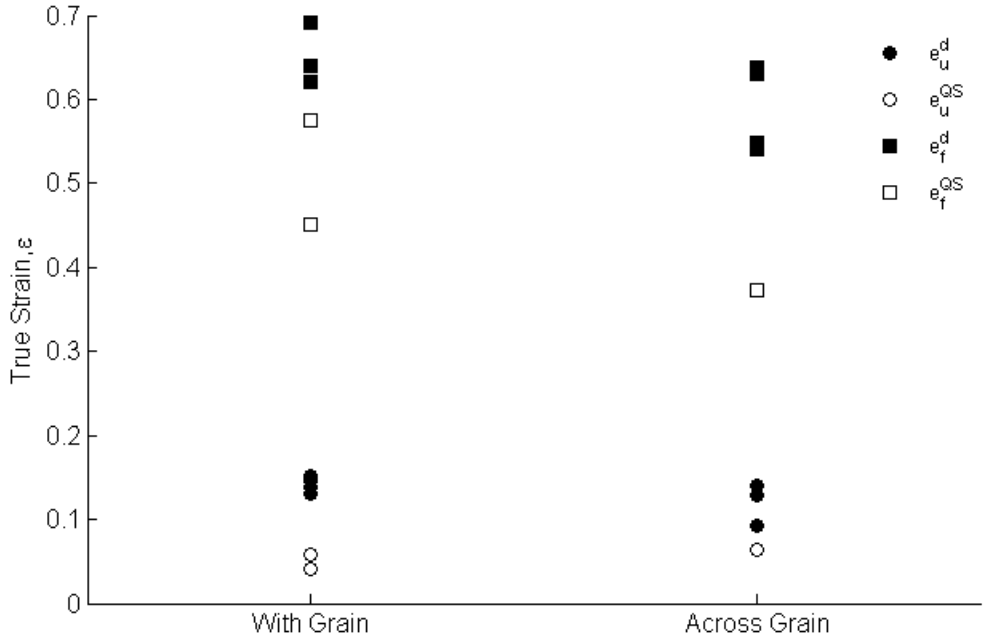

Figure 2.11: Uniform and failure strains for Al 6061-T6

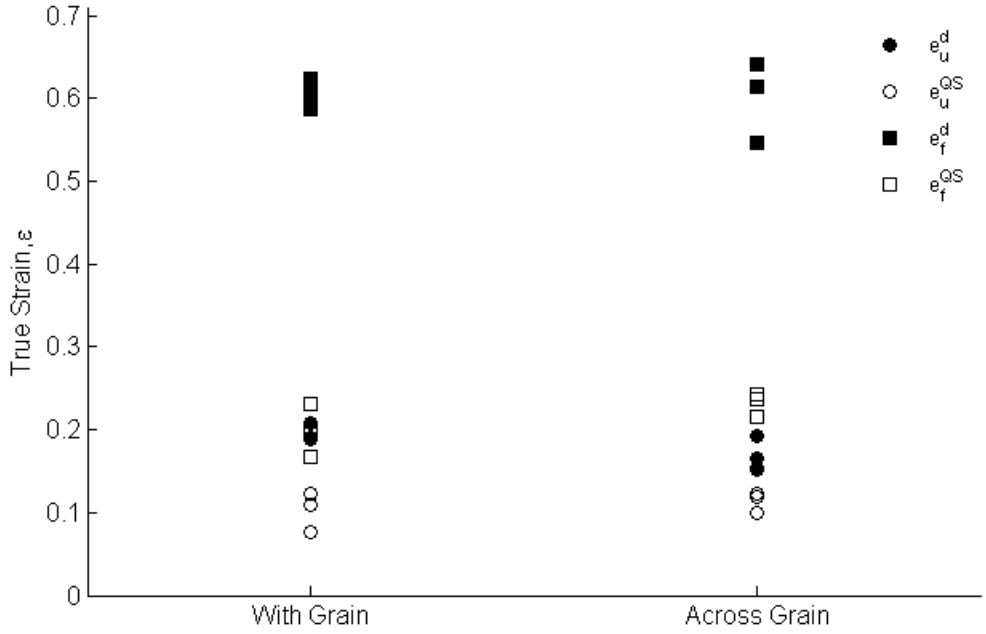

Figure 2.12: Uniform and failure strains for Al 5083-H116

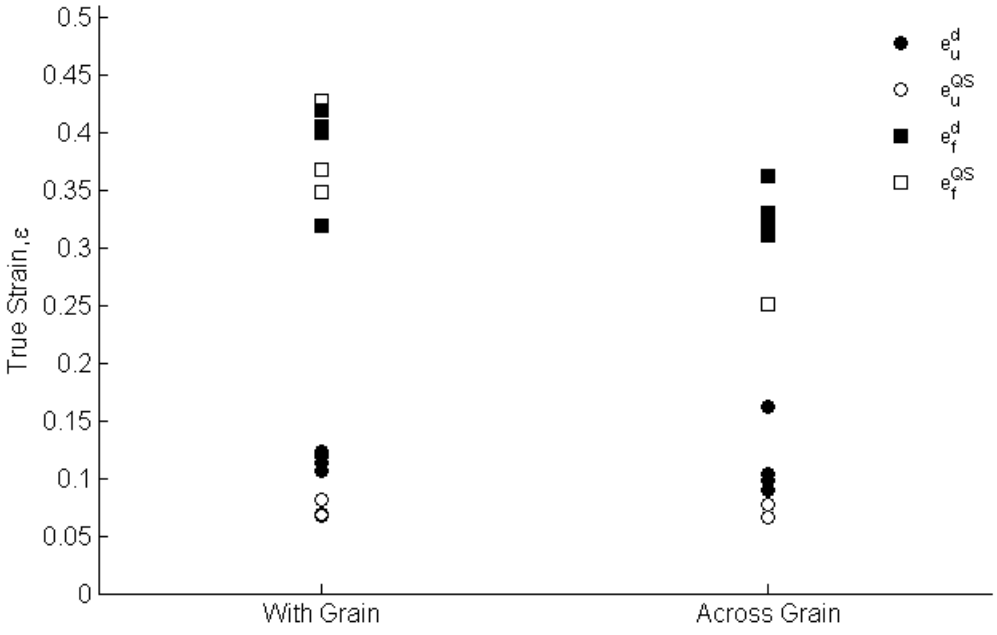

Figure 2.13: Uniform and failure strains for Al 7075-T73

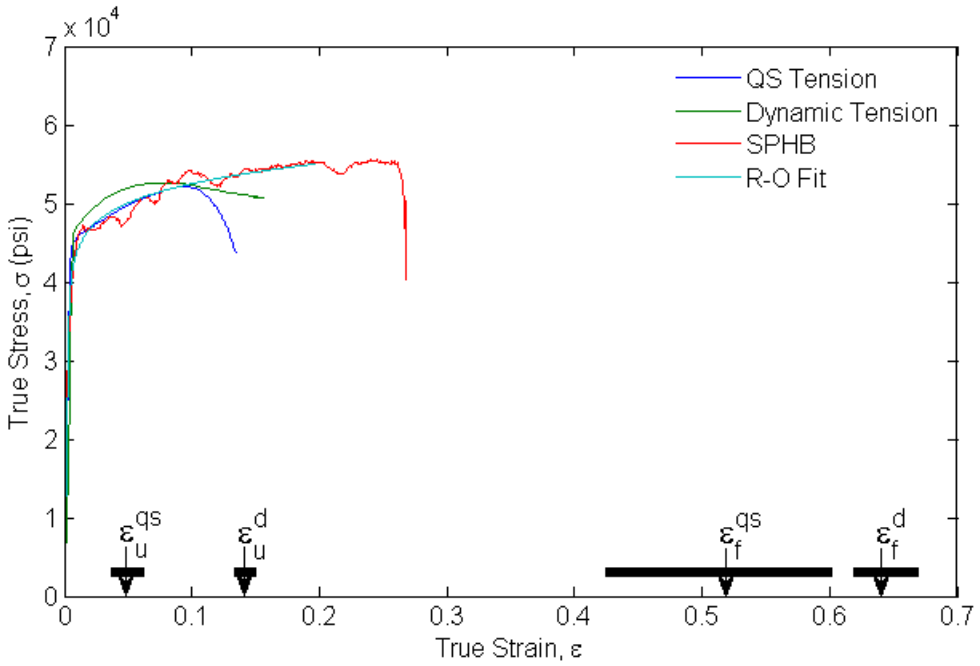

Figure 2.14: Master plot for Al 6061-T6-W

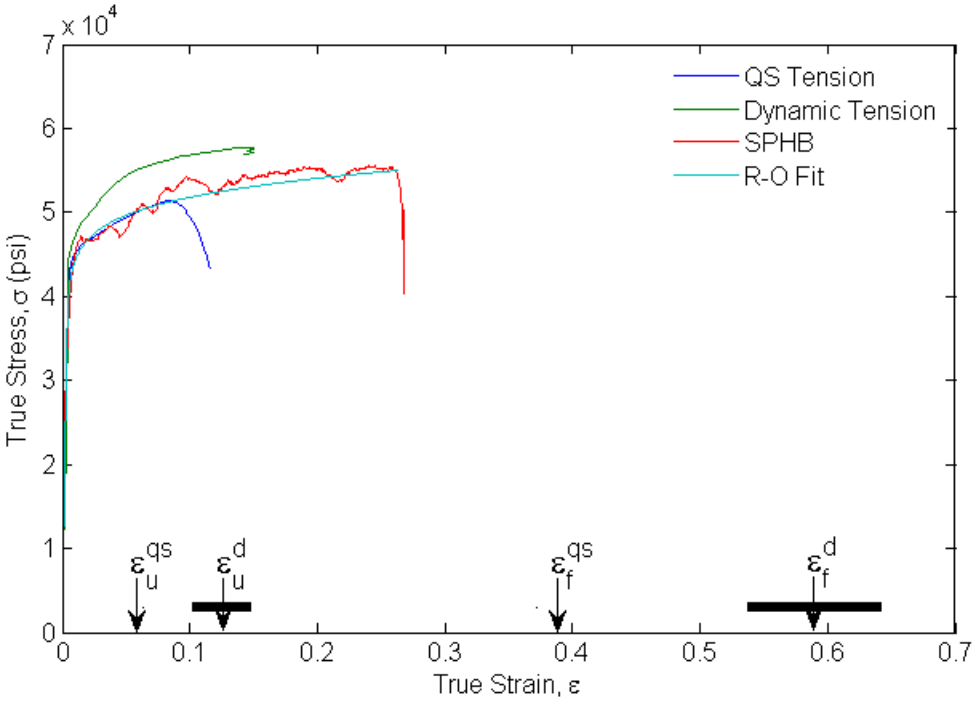

Figure 2.15: Master plot for Al 6061-T6-A

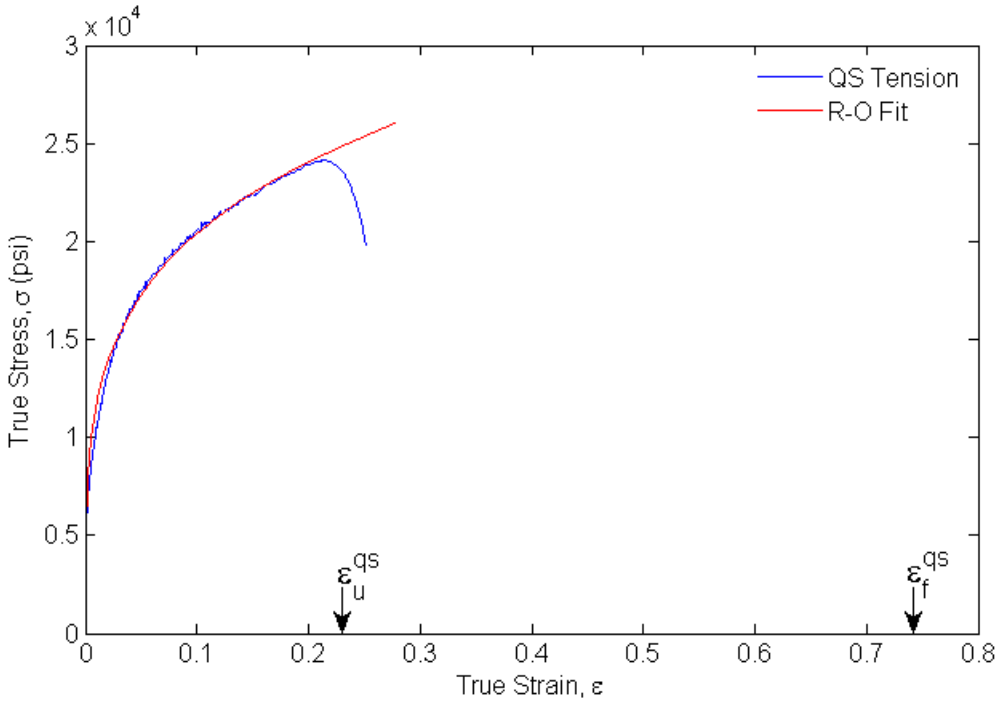

Figure 2.16: Master plot for Al 6061-O

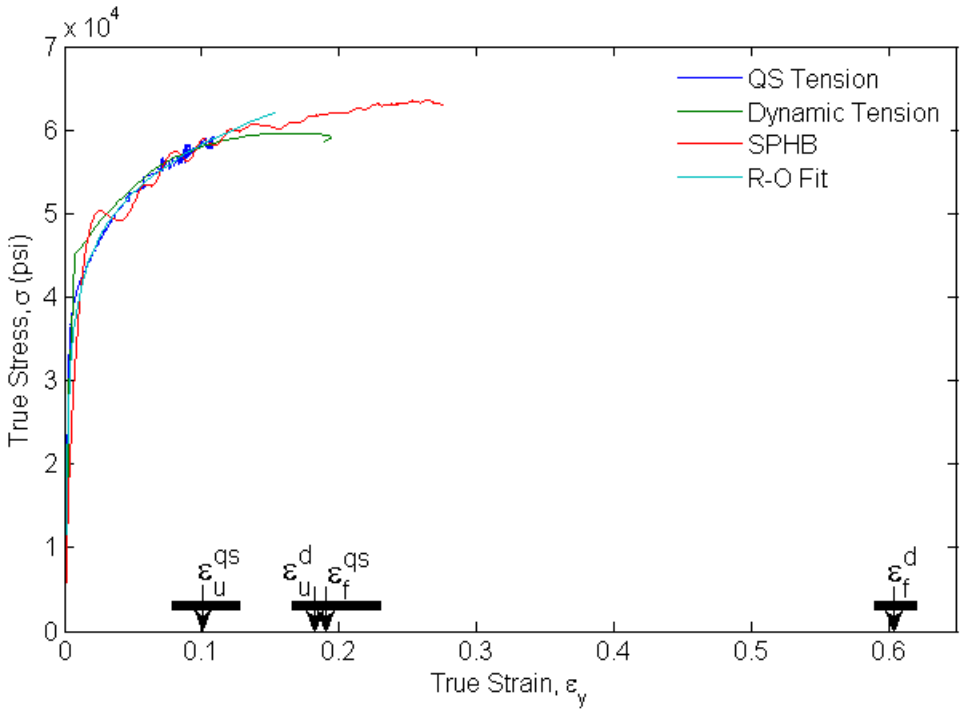

Figure 2.17: Master plot for Al 5083-H116-W

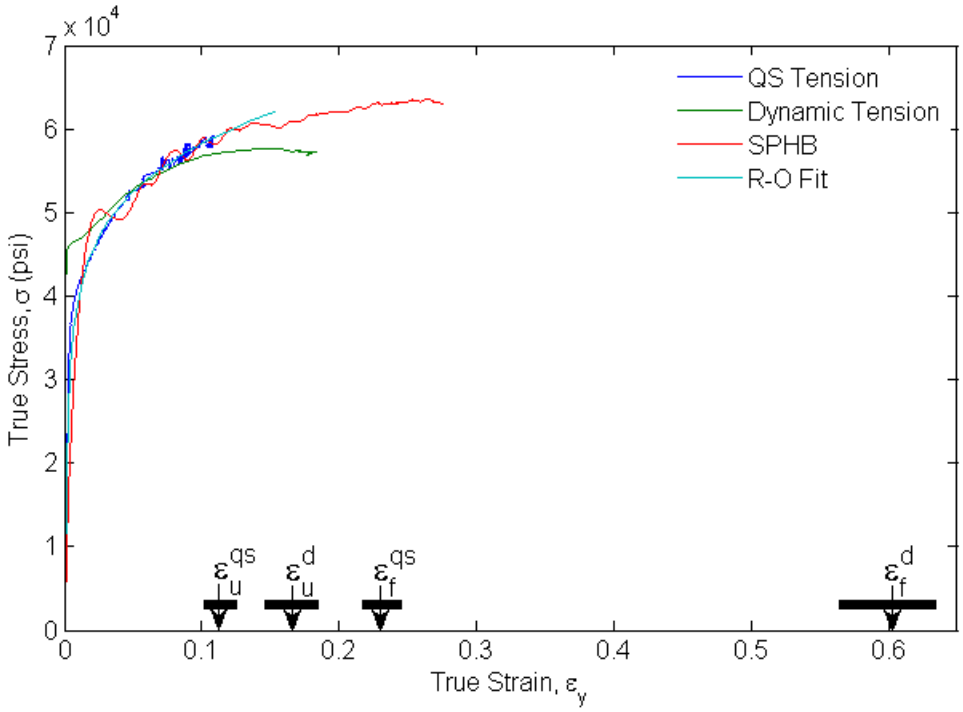

Figure 2.18: Master plot for Al 5083-H116-A

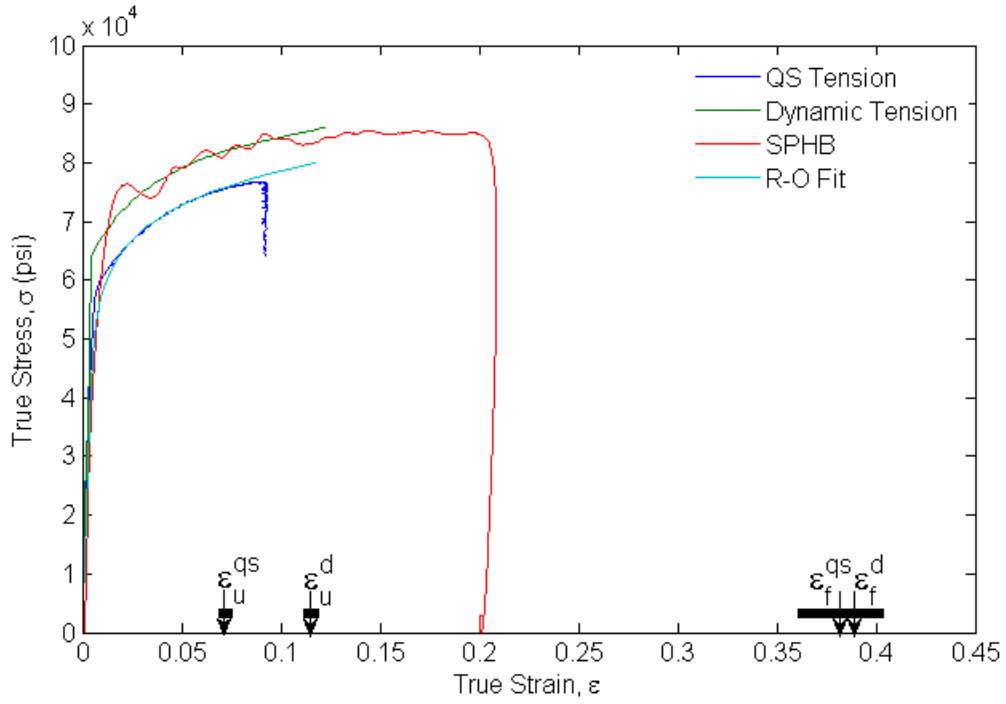

Figure 2.19: Master plot for Al 7075-T73-W

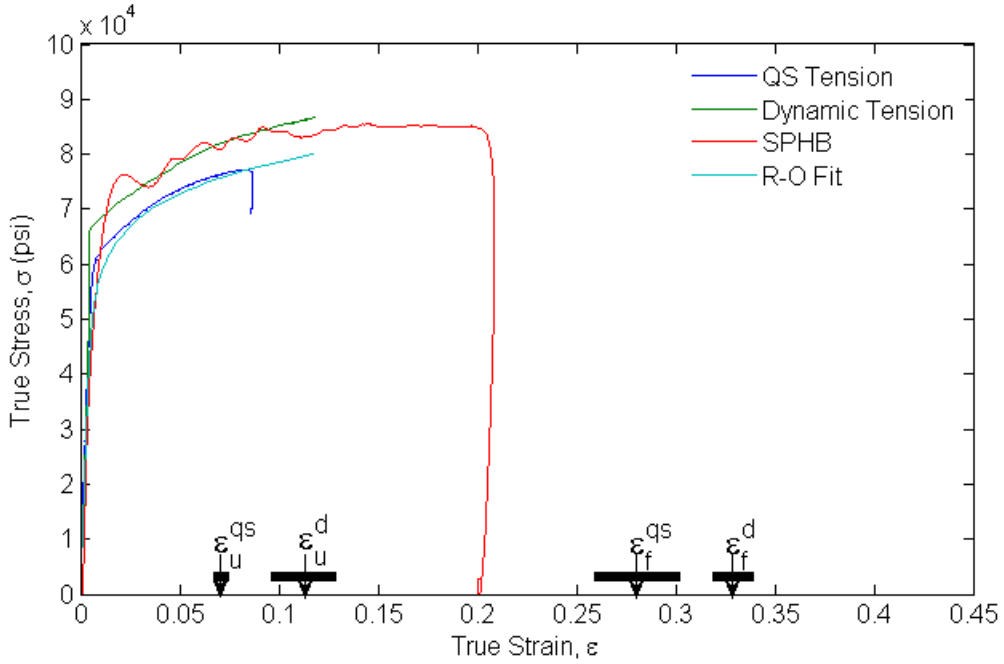

Figure 2.20: Master plot for Al 7075-T73-A

Chapter 3: Ductile Fracture

In most engineering materials, fracture falls into one of two broad categories: brittle or ductile. In brittle fracture, the crack tip does not undergo significant deformation, and an elastic analysis is usually appropriate and adequate. The primary parameter of concern in the elastic fracture problem is the stress intensity factor. The linear elastic fracture boundary value solution is referred to as the K-field due to the dominance of the stress intensity factor in the solution.

When a ductile material experiences fracture, the crack tip region undergoes significant plastic deformation. Small scale yielding occurs when the material deforms plastically in a small region in relation to the thickness and width of the structure. ASTM standard E-1820 outlines the conditions necessary for small scale yielding:

$$t, W > 2.5\left(\frac{K_{Ic}}{\sigma_y}\right)^2 \tag{3.1}$$

If the small-scale yielding condition is satisfied, the plastic zone is insignificant in relation to the width and thickness, plane strain conditions prevail, and a linear-elastic analysis will suffice. If the stress intensity factors found in Section 3.6 are used, the necessary conditions for small scale yielding are 0.144 m for Al 6061-T6 and 6.44 m for Al 6061-O! It is well known that the small-scale yield condition is particularly difficult to satisfy in low strength, high toughness materials. Many structures do not meet the small-scale yield criterion and must be analyzed by incorporating effects of large-scale plastic deformation in the analysis. Even if a valid fracture toughness value can be found using

the small-scale yield condition, many structures are still manufactured using thin sheets where large scale yielding exists.

In this investigation of thin aluminum plates, large scale yielding is prevalent, plane stress conditions are dominant, and in order to account for the large scale yielding, a full elastic-plastic analysis is necessary. Similar to the stress intensity factor of the linear elastic problem, the elastic-plastic problem is characterized by employing the J-integral.

Rice (1968) proposed the J-integral to calculate the energy release rate for any arbitrary geometry, and the J-integral has been a useful tool in characterizing elastic-plastic fracture. The J-integral is a path independent contour integral around the crack tip that is valid until crack initiation. In order to establish a fracture criterion, the value of the J-integral at crack initiation will be considered to be the critical J-integral, or J_c.

Sutton, et al (1992), used digital image correlation to compute the J-integral locally in plane stress SENT specimens of PMMA. However, in their calculations, the material behavior was linear elastic, and the J-integral was written in terms of displacement gradients and *elastic* material property parameters. The calculations were simplified by using rectangular contours for the J-integral calculation.

In a similar study, Kang, et al (2005), used digital image correlation to calculate the plane stress J-integral in copper foils. Their experimental procedure was very similar to Sutton, et al (1992), but they characterized their material using the Ramberg-Osgood power-law hardening model, even though all their calculations were linear elastic. No plasticity was accounted for in the computation of the J-integral. Square contours were

also used to simplify the calculations. A finite summation over square contours was used in place of numerical integration to calculate the J-integral.

For our tests, the aluminum alloy 6061 was tested in both the T6 and annealed O conditions.

3.1 Fracture Tests

Fracture test specimens with the geometry shown in Figure 3.1a were created from the aluminum sheet stock. The initial crack of length $a_o = 7.6$ mm was created using the EDM wire cutting. The length of the gripped section is G, and h is the length of the section from the crack to the gripped section.

Each specimen was loaded cyclically in load control in the MTS machine until a fatigue crack started to propagate from the EDM notch. The mean stress during cyclic loading was kept at a minimum as to not create a large zone of plastic deformation in the specimens as specified in ASTM 1820. Once the fatigue cracks reached a length of 1 to 3 millimeters, the cyclic loading was stopped. The lengths of the fatigue cracks were measured after the fracture tests were completed and are shown in Table 3.1.

After proper fatigue pre-cracking, the specimens were painted with a stochastic speckle pattern for implementation of digital image correlation measurements and tested. An Instron 4482 machine was used in displacement control at a rate of 0.01 inches per minute, and the Instron Series IX software was used to control and record the load and crosshead displacement. The Aramis DIC hardware and software were used to capture images at 1 frame per second of the fracture specimens, as they were loaded to failure.

The field of view of the camera was set to 15 mm by 10 mm in order to focus attention on the region near the crack tip. In order to determine the crack mouth opening displacement CMOD, a second camera was used to record images over a larger field of view where the specimen edges could be observed; the CMOD is defined in Figure 3.1b.

The Aramis DIC software was used to calculate the displacement and strain fields within the field of view of the specimen, and upon completion, the stress field was calculated from the Aramis data.

Additionally, a large-scale fracture test was performed on the Al 6061-T6. For this test, a SENT specimen with a 5 inch notch and a 5 inch ligament length (SENT-5-5) was loaded in a custom designed loading attachment to the Intron 4482 machine. Images were recorded using the Nikon D90 camera and analyzed with the Aramis software. The crack length was found by processing the images with a MATLAB routine.

3.2 Determination of Stress from DIC

For the fracture tests, the Aramis DIC software package was used to find the displacement and strain fields of a series of images. In order to determine the J-integral from these measurements, it is necessary to determine the stress field as well. Since the material deforms plastically, this requires a separation of the total strain into its elastic and plastic parts, as well as a determination of the current effective stress. In general, the plastic constitutive behavior of a material is modeled using the second and third invariants of the deviatoric stress tensor, $\varepsilon_{ij}^{p} = \phi\left(J_2, J_3\right)s_{ij}$. In the case of the von Mises yielding, the material behavior is dependent only upon the second invariant:

$$\varepsilon_{ij}^{p} = \phi(J_2)s_{ij} \tag{3.2}$$

This corresponds to the J_2-deformation theory of plasticity and is used to calculate the stress field. Now the total strain can be decomposed into the plastic and elastic stains, and in the case of uniaxial tension, Eq. (3.2) becomes

$$\varepsilon_{11}^{p} = \varepsilon_{11} - \varepsilon_{11}^{e} = \left(\frac{1}{E_s} - \frac{1}{E}\right)\sigma_{11} \tag{3.3}$$

where E is Young's modulus and E_s is the secant modulus. The yield function is found by combining Eqs. (3.2) and (3.3).

$$\varepsilon_{ij}^{p} = \left(\frac{1}{E_s} - \frac{1}{E}\right)s_{ij} \tag{3.4}$$

Furthermore, by rewriting the strain in terms of the elastic and plastic components, the stress strain relationship becomes a sum of the elastic and plastic parts.

$$\varepsilon_{ij} = \frac{1+v}{E}\sigma_{ij} - \frac{v}{E}\sigma_{kk}\delta_{ij} + \frac{3}{2}\left(\frac{1}{E_s} - \frac{1}{E}\right)s_{ij} \tag{3.5}$$

The first two terms make up the linear elastic components of strain, and the third term is the plastic component from Eq. (3.4). The J_2-deformation theory of plasticity is appropriate for this calculation because proportional loading occurs during elastic and plastic deformation. Unloading in the specimen would make this calculation invalid, but we limit this investigation only up to the stage of crack initiation. For these tests, plane stress ($\sigma_{33} = 0$) is assumed, and Eq. (3.5) can be expanded for each strain component.

$$\varepsilon_1 = \frac{1}{E_s}(\sigma_1 - v_s\sigma_2)$$

$$\varepsilon_2 = \frac{1}{E_s}(\sigma_2 - v_s\sigma_1) \tag{3.6}$$

$$\varepsilon_3 = \frac{v_s}{E_s}(\sigma_1 + \sigma_2)$$

Additionally, σ_1 and σ_1 can be written in terms of ε_1 and ε_2 by combining the first two Eqs. (3.6), which consequently allows ε_3 to be written in terms of ε_1 and ε_2.

$$\varepsilon_3 = -\frac{v_s}{1 - v_s}(\varepsilon_1 + \varepsilon_2) \tag{3.7}$$

The material is assumed to become incompressible after it becomes plastic, and Poisson's ratio gradually increases from 0.33 to 0.5.

$$v_s = \frac{1}{2} + \frac{E_s}{E}\left(v - \frac{1}{2}\right) \tag{3.8}$$

In order to generalize to multiaxial stress states, the equivalent stress and equivalent plastic strain must be defined in terms of the stress and strain components. The uniaxial stress and strain state is replaced by the multiaxial stress and strain state through these equivalent quantities. The von Mises or equivalent stress and the equivalent plastic strain are defined as

$$\sigma_e^2 = \frac{3}{2}s_{ij}s_{ij} \tag{3.9}$$

$$\varepsilon_e^p = \sqrt{\frac{2}{3}\varepsilon_{ij}^p\varepsilon_{ij}^p} \tag{3.10}$$

With the quantities defined in Eqs. (3.9) and (3.10), Eq. (3.4) can be generalized to represent the equivalent stress and equivalent plastic strain.

$$\varepsilon_e^p = \left(\frac{1}{E_s} - \frac{1}{E}\right)\sigma_e \tag{3.11}$$

The secant modulus E_s can be calculated easily for any hardening model and used in the above expression. For the particular example considered here, a Ramberg-Osgood fit will be used to characterize the stress-strain response of the material (as shown in Section 2.2). The power law model is then used to find the secant modulus:

$$E_s(\sigma_e) = E\left[1 + \alpha\left(\frac{\sigma_e}{\sigma_y}\right)^{n-1}\right]^{-1} \tag{3.12}$$

Note that the secant modulus is a function of only the equivalent stress. With the displacements u_1 and u_2 and the strains ε_1 and ε_2 obtained from the DIC measurements, it is required to estimate the equivalent stress in order to determine E_s and v_s in order to determine the plastic components of strain. By substituting $\varepsilon_{kk} = \sigma_{kk}/3K$ into Eq. (3.5) and "multiplying" it by itself, an equation in terms of the strains and equivalent stress can be written:

$$\varepsilon_{ij}\varepsilon_{ij} - \frac{\varepsilon_{kk}^2}{3} = \frac{2}{3}\left[\frac{1+v}{E} + \frac{3}{2}\left(\frac{E - E_s}{EE_s}\right)\right]^2 \sigma_e^2 \tag{3.13}$$

Nothing that the left hand side is in terms of the measured total strains and from Eq. (3.12), that E_s is a function only of the effective stress, it is clear that Eq. (3.13) can be solved numerically for the equivalent stress. The result can be used to calculate the secant modulus E_s and the effective Poisson's ratio v_s. The Matlab function *fzero* is used to

determine the value of the equivalent stress from Eq. (3.13). By inverting Eqs.(3.6), the stress components can be calculated in terms of the strains.

$$\sigma_1 = \frac{E_s}{1 - v_s^2}(\varepsilon_1 + v_s\varepsilon_2)$$
$$\sigma_2 = \frac{E_s}{1 - v_s^2}(\varepsilon_2 + v_s\varepsilon_1) \tag{3.14}$$

The stresses in Eqs. (3.14) are the principal stresses, and consequently the stresses in the original frame can also be found by using the strains in the original frame:

$$\sigma_{11} = \frac{E_s}{1 - v_s^2}(\varepsilon_{11} + v_s\varepsilon_{22})$$
$$\sigma_{22} = \frac{E_s}{1 - v_s^2}(\varepsilon_{22} + v_s\varepsilon_{11}) \tag{3.15}$$
$$\sigma_{12} = \frac{2EE_s}{2vE_s - E_s + 3E}\varepsilon_{12}$$

Eqs. (3.15) allow the complete determination of the elastic-plastic stress and strain state at every point throughout the field of view and hence permit the calculation of the J-integral through any contour around the crack tip. We note that a corresponding development can be made for the J_2 incremental theory of plasticity.

3.3 THE J-INTEGRAL AS A LINE INTEGRAL

The J-integral for any arbitrary geometry is a contour integral around the crack tip.

$$J = \int_\Gamma \left(Wn_1 - T_\alpha \frac{\partial u_\alpha}{\partial x_1}\right) ds \tag{3.16}$$

Where W is the strain energy, T_α are the components of the traction vector, u_α are the displacement components and ds is the length increment along the contour Γ. The strain energy is a measure of the work done on the nonlinear material during loading to a strain level $\varepsilon_{\alpha\beta}$ is:

$$W = \int_0^{\varepsilon_{\alpha\beta}} \sigma_{\alpha\beta} d\varepsilon_{\alpha\beta} \tag{3.17}$$

There are many different methods of extracting the J-integral from the experiments. First, for conditions of small scale yielding, one could use an estimate based on the stress intensity factor. Second, under conditions of large scale nonlinear deformations, a global analysis based on load and load-line displacement measurements can be used to determine J. Lastly, the local stress and strain fields identified through the DIC procedure discussed above can be used to evaluate Eq. (3.16); these are discussed in reverse order. The strain component in Eq. (3.17) is separated into the elastic and plastic part. The plastic strain is known from the power law curve.

$$\varepsilon_{\alpha\beta}^p = \frac{3}{2}\alpha\left(\frac{\sigma_e}{\sigma_y}\right)^{n-1}\frac{s_{\alpha\beta}}{\sigma_y} \tag{3.18}$$

The elastic strain energy is easily integrated to yield:

$$W = \sigma_e \varepsilon_e^e = \frac{\sigma_e^2}{2E} \tag{3.19}$$

After differentiation and algebraic manipulation, the total strain energy can be written as:

$$W = \frac{\sigma_e^2}{2E} + \frac{n}{n+1}\sigma_e \varepsilon_e^p \tag{3.20}$$

The tractions T_α are the normal stresses acting at the boundary of the contour.

$$T_\alpha = \sigma_{\alpha\beta} n_\beta \tag{3.21}$$

The stress components $\sigma_{\alpha\beta}$ are known from the stress analysis presented above, and n_β are components of the unit vector normal to the contour Γ. For simplicity, the contour Γ around the crack tip used in our calculation of the J-integral is rectangular shaped. For the rectangular shaped contours, the J-integral is decomposed into four distinct sections.

$$\begin{aligned}
\Gamma_1: J &= -\int W dy + \int \left(\sigma_{11}\frac{\partial u}{\partial x} + \sigma_{12}\frac{\partial v}{\partial x}\right) dy \\
\Gamma_2: J &= \int \left(\sigma_{12}\frac{\partial u}{\partial x} + \sigma_{22}\frac{\partial v}{\partial x}\right) dx \\
\Gamma_3: J &= \int W dy - \int \left(\sigma_{11}\frac{\partial u}{\partial x} + \sigma_{12}\frac{\partial v}{\partial x}\right) dy \\
\Gamma_4: J &= -\int \left(\sigma_{12}\frac{\partial u}{\partial x} + \sigma_{22}\frac{\partial v}{\partial x}\right) dx
\end{aligned} \tag{3.21}$$

These contours are illustrated in Figure 3.2. The total value of the J-integral is the summation of *J* along all four sides of the contour.

$$J = J_{\Gamma_1} + J_{\Gamma_2} + J_{\Gamma_3} + J_{\Gamma_4} \tag{3.22}$$

Additionally, the J-integral can be derived and calculated using the load and displacement measurements:

$$J = \frac{1}{bt}\int_0^\Delta P d\Delta \tag{3.23}$$

In Eq. (3.23), b is the ligament length of the specimen, and t is the specimen thickness. The value of J calculated from the load displacement curve will be used as a comparison for the J-integral calculated from the DIC measurements. Note, however, that this does not include corrections for load-train compliance or specimen geometry effects.

The LEFM stress intensity factor for the SENT specimen is given as (see for example, Zehnder 2009):

$$K_I = \sigma\sqrt{\pi a}\left[0.265\left(1-\frac{a}{W}\right)^4 + \frac{0.857+0.265\frac{a}{W}}{\left(1-\frac{a}{W}\right)^{3/2}}\right] \tag{3.24}$$

For Eq. (3.24) to be valid, the ratio h/W must be greater than 1, where h is the height of the specimen from the crack to the upper/lower grip. Prior to crack initiation, the stress is the only parameter that changes during an experiment, and the critical value of the stress intensity factor K_{Ic} is found by using the load at the instant of crack initiation to compute the stress in Eq. (3.24). For the linear elastic problem, the value of J can be written in terms of the stress intensity factor.

$$J = \frac{K_I^2}{E} \tag{3.25}$$

When using thin aluminum sheets to design fracture critical structures, the LEFM stress intensity factor leads to very conservative design because the K-field fracture criterion is much smaller than the actual J-integral at initiation. This is demonstrated by comparing the J-integral calculations in this study to the LEFM stress intensity factor for SENT specimens. Values of the critical J-integral calculated using Eqs. (3.16), (3.23) and (3.24) are compared in Table 3.1.

3.4 The J-Integral as an Area Integral

An expression for the J-integral as an area integral has been derived for use in the case of no thermal strains, body forces, or crack face tractions (Needleman, et al 1985).

$$J = \int_A \left[\sigma_{ij} u_{j,1} - W\delta_{1i}\right] q_{1,i} dA \tag{3.26}$$

The displacements are given from the DIC, the stresses have already been calculated using the procedure in Section 3.2, and the work W was calculated according to Eq. (3.20). The expression in brackets is weighted by the parameter q. For the area integral, the contour is weighted because the contour has a value of one on the inner boundary, and a value of zero on the outer boundary. A gradient exists between the inner and outer contour boundaries, and $q_{1,i}$ is the gradient at any calculation point inside the area of integration. For ease of computation, the contours are squares, shown in Figure 3.3. The expression for the J-integral was derived for square contours, and the integration is performed through the means of a finite summation in both x and y directions.

3.5 Verification of J-Integral Code

In order to verify the results from the J-integral calculation, the two dimensional linear elastic crack-tip field was numerically generated for Mode-I. A comparison between the K-field solution input and the different J-integral contours shows small differences. The J value input divided by the calculated value from the routine described in Section 3.3 was found to be ~0.9945. There exists less than 1% difference in the computed value and the actual value.

3.6 Experimental Results

Contours of the strain components obtained from experiments and the effective stress calculated using the J_2-deformation theory are plotted in Figures 3.4 and 3.5 for

different load levels before crack initiation for the Al 6061 in the T6 and O conditions, respectively. These plots are intended to provide a qualitative comparison of differences in the strain and equivalent stress contours of the two materials. These plots show significant differences in the way the plastic zone develops near the crack tip in the two different materials. In the Al 6061-O, the material with a high hardening exponent, the shape of the zone of intense plastic deformation appears similar to estimates for a plane strain calculation based on the K-field. In contrast, the shape of the plastic zone appears to be more localized along two directions for Al 6061-T6. This difference has significance in the manner in which fracture develops, as we shall explore later.

Plots of the load vs. CMOD are shown in Figures 3.6 and 3.7 for three different tests for Al 6061-T6 and two different tests for Al 6061-O. These plots show an early region of linear deformation followed by a later region of non-linear response. The onset of crack initiation (identified optically from high magnification views of the DIC images, at a resolution of 0.5 mm) is indicated by a filled circular symbol in each curve. The consistency of the load trace between the tests attests to the high degree of repeatability; the only variation appears to be in the onset of crack initiation.

Following the CMOD calculations, the J-integral was calculated for different tests using Eq. (3.23) and is plotted in Figures 3.10 and 3.11. The two different tests of the Al 6061-T6 are very similar in nature; however, the load at failure is lower for QSF6061-T6-07. The solid circular markers denote the J-integral at failure. The failure stage was found by optical inspection of the images recorded for DIC. The critical value of J for the Al 6061-T6 material is found to be approximately 80 kJ/m^2. It is notable that there is a rather

steep increase in the value of J around this point; a small error in identification of crack onset could result in a significant increase in the estimate of the value of J for initiation. It is also important to note that this critical value of J is significantly larger than the corresponding value obtained from plane strain conditions as shown in Table 3.1.

The load vs. J-integral plots for the Al 6061-O material agree very well with one another as shown in Figure 3.9. The critical value of J is slightly different for the two tests; however, as previously discussed, the identification of the onset of crack extension is extremely important in controlling the variability in the critical fracture toughness. For the Al 6061-O material, the critical value of J is approximately 110 kJ/m^2. This value is substantially greater than the Al 6061-T6 suggesting that the fracture energy is significantly decreased by the aged microstructure of the T6 heat treatment.

In addition to the estimate of the J-integral based on the global load displacement measurements, the local DIC measurements were used, following the procedure discussed in Section 3.3 to estimate the J-integral along specific contours around the crack tip. Three different contours were considered as illustrated in Figures 3.10 and 3.11 for the Al 6061-T6 and –O, respectively. Note that these contours are symmetric with respect to the crack-tip. The color maps correspond to the von Mises effective stress and indicate that the J-integral contours go through the plastically deformed regions of the crack tip neighborhood. The variations of the J-integrals for the different contours for both materials are shown in Figures 3.12 and 3.13. The J-integral calculations are practically identical over the different contours when plotted with the load. For square contours symmetric about the crack-tip, the J-integral is indeed path-independent.

Comparisons of the variation of the J with load calculated from the load-CMOD measurements and from the DIC measurements of the strain field are shown in Figures 3.14 and 3.15 for QSF-6061-T6-06 and QSF-6061-O-04. The load-displacement formulation does over predict the value of the J-integral; however, we have not accounted for specimen geometric effects in the estimate based on Eq. (3.23).

For the large-scale fracture test, the J-integral was calculated using the area integral form, and the change in crack length da was found. The test set-up is shown in Figure 3.16. Shown in Figure 3.17, the *J* vs. da was plotted with similar results from the small SENT specimens (shown in Figure 3.1). For the large tests, the J-integral ceases to increase as the crack propagates. Therefore, steady state crack propagation occurs for a *J* value of $\sim 150\ kJ/m^2$. For the small test specimen, the *J* value continues to increase the as the crack propagates, thus never reaching a steady state value. This can be attributed to the ability of the grips to constrain the rotation of the specimen as the crack propagates past the load line of the text fixture. As the crack propagates, the specimen rotates and the J-integral values continue to increase.

3.7 MEASUREMENTS COMPARED WITH HRR FIELDS

The measured variation of the crack tip strain fields are in the elastic-plastic range; having estimated the local values of the J-integral and demonstrated the path-independence of the J-integral, we turn to a comparison of the measured strain-fields to the estimates based on the HRR field. In the HRR model, the strength of the singularity at

the crack-tip is determined by the strain hardening parameter, n. The procedure for solving the HRR fields for Mode I loading was taken from Kanninen and Popelar (1985).

The elastic strain component of Eq. (3.5) is neglected in the crack tip region since the elastic strain is negligible when compared with the plastic strain.

$$\varepsilon_{ij} = \frac{3}{2}\alpha\varepsilon_y \left(\frac{\sigma_e}{\sigma_y}\right)^{n-1} \frac{s_{ij}}{\sigma_y} \tag{3.30}$$

If the stress and strain are assumed to be separable in terms of r and θ, then the stresses, strains and displacements take the form of Eqs. (3.31).

$$\begin{aligned} \sigma_{ij}(r,\theta) &= Kr^{-1/(n+1)}\tilde{\sigma}_{ij}(\theta) \\ \sigma_e(r,\theta) &= Kr^{-1/(n+1)}\tilde{\sigma}(\theta) \\ \varepsilon_{ij}(r,\theta) &= \alpha\varepsilon_y K^n r^{-n/(n+1)}\tilde{\varepsilon}_{ij}(\theta) \\ u_i(r,\theta) &= \alpha\varepsilon_y K^n r^{1/(n+1)}\tilde{u}_i(\theta) \end{aligned} \tag{3.31}$$

Where K is the plastic intensity factor. The tilde over stresses and strains signifies dependence only upon theta. For a linear elastic material $n = 1$, and Eqs. (3.31) have the square root of r singularity as seen in the K-field solution. In order to solve Eqs. (3.31), a separable Airy stress function is employed to reduce the problem into the solution of a function with dependence upon one unknown.

$$\Psi = Kr^{(2n+1)/(n+1)}\tilde{\Psi}(\theta) \tag{3.32}$$

The solution of the problem is simplified by polar coordinates. The stresses are written in terms of the Airy stress function accordingly.

$$\sigma_{\theta\theta} = \frac{\partial^2 \Psi}{\partial r^2} = Ks(s-1)r^{-1/(n+1)}\tilde{\Psi}(\theta)$$

$$\sigma_{rr} = \frac{1}{r}\frac{\partial \Psi}{\partial r} + \frac{1}{r^2}\frac{\partial^2 \Psi}{\partial \theta^2} = K(1-s)r^{-1/(n+1)}\tilde{\Psi}'(\theta) \tag{3.33}$$

$$\sigma_{r\theta} = -\frac{\partial}{\partial r}\left(\frac{1}{r}\frac{\partial \Psi}{\partial \theta}\right) = Kr^{-1/(n+1)}\left[s\tilde{\Psi}(\theta) + \tilde{\Psi}''(\theta)\right]$$

The prime signifies differentiation with respect to theta, and $s = (2n+1)/(n+1)$. For the Airy stress function to be permissible, the strain compatibility condition must be satisfied.

$$\frac{1}{r}\frac{\partial^2}{\partial r^2}(r\varepsilon_{\theta\theta}) + \frac{1}{r^2}\frac{\partial^2 \varepsilon_{rr}}{\partial \theta^2} - \frac{1}{r}\frac{\partial \varepsilon_{rr}}{\partial r} - \frac{2}{r^2}\frac{\partial}{\partial r}\left(r\frac{\partial \varepsilon_{r\theta}}{\partial \theta}\right) = 0 \tag{3.34}$$

The strain components are found by combining Eqs. (3.33) and (3.30), and the strains then are substituted into Eq. (3.34). The strain compatibility condition is now written in terms of the power law hardening exponent n, $\tilde{\sigma}$ and $\tilde{\Psi}$.

$$\left[\frac{d^2}{d\theta^2} + \frac{n}{n+1}\right]\left[\tilde{\sigma}^{n-1}\left(2\tilde{\Psi}'' + \frac{n+2}{n+1}\frac{2n+1}{n+1}\tilde{\Psi}\right)\right] + \frac{n}{(n+1)^2}\tilde{\sigma}^{n-1}\left(\tilde{\Psi}'' - \frac{n-1}{n+1}\frac{2n+1}{n+1}\tilde{\Psi}\right) + \frac{6n}{(n+1)^2}\left(\tilde{\sigma}^{n-1}\tilde{\Psi}'\right)' = 0 \tag{3.35}$$

The function $\tilde{\sigma}$ is the theta dependent part of the equivalent stress and is in terms of the Airy stress function and the hardening exponent n.

$$\tilde{\sigma} = \left(\tilde{\sigma}_{rr}^2 + \tilde{\sigma}_{\theta\theta}^2 - \tilde{\sigma}_{rr}\tilde{\sigma}_{\theta\theta} + 3\tilde{\sigma}_{r\theta}^2\right)^{\frac{1}{2}}$$
$$= \left\{\left[\tilde{\Psi}'' + s\tilde{\Psi}\right]^2 + \left[s(s-1)\tilde{\Psi}\right]^2 - s(s-1)\left[\tilde{\Psi}'' + s\tilde{\Psi}\right]\tilde{\Psi} + 3\left[(1-s)\tilde{\Psi}'\right]^2\right\}^{1/2} \tag{3.36}$$

After substituting Eq. (3.36) into Eq. (3.35), the latter can be solved numerically for $\widetilde{\Psi}$ after prescribing proper boundary conditions. For this exercise, the crack surfaces must be traction free.

$$\begin{gathered}\sigma_{r\theta}(r,\pm\pi)=0\\ \sigma_{\theta\theta}(r,\pm\pi)=0\\ \widetilde{\Psi}(\pm\pi)=0\\ \widetilde{\Psi}'(\pm\pi)=0\end{gathered} \tag{3.37}$$

Furthermore, the plastic intensity factor K can be replaced with J, and the HRR field equations reduce to:

$$\begin{gathered}\sigma_{\alpha\beta}=\left(\frac{J}{\alpha\varepsilon_y\sigma_y I_n r}\right)^{\frac{1}{n+1}}\tilde{\sigma}_{\alpha\beta}(\theta)\\ \varepsilon_{\alpha\beta}=\alpha\varepsilon_y\left(\frac{J}{\alpha\varepsilon_y\sigma_y I_n r}\right)^{\frac{n}{n+1}}\tilde{\varepsilon}_{\alpha\beta}(\theta)\\ u_\alpha=\alpha\varepsilon_y\left(\frac{J}{\alpha\varepsilon_y\sigma_y I_n r}\right)^{\frac{n}{n+1}}r^{1/n+1}\tilde{u}_\alpha(\theta)\\ \varepsilon_{\alpha 3}=0 \qquad\qquad \sigma_{\alpha 3}=0\end{gathered} \tag{3.38}$$

For plane stress, σ_{33} is equal to zero, and ε_{33} is equal to $-(\varepsilon_{11}+\varepsilon_{22})$. Here, the value of J is determined through the J-integral calculation as outlined in Chapter 3.

The experimental stress fields for each alloy are compared with the HRR predictions and shown in Figure 4.20 and Figure 4.21. These results further demonstrate that the HRR field approximations fail to capture the slant fracture plastic zone size and shape.

Furthermore, the differences between the plastic zone shapes in Eqs. (3.38) for two different strain hardening materials are fundamentally no different. The hardening exponent and J are the only two parameters in these equations. The hardening exponent does change the singularity at the crack tip but does not alter the overall shape of the plastic field. In the numerical analysis of slant fracture, this model has obvious limitations near the crack tip.

When compared to the experimental results, it becomes evident that the HRR fields do not properly capture the plastic zone shapes or equivalent stress levels as shown in Figures 3.20 and 3.21. In Figure 3.20, the equivalent stress contours for the Al 6061-T6 material are compared with the HRR field at several different levels of *J*. (The HRR fails to capture the slant fracture plastic zone shape early in the loading, and the intensity of the stress levels are significantly overestimated. The HRR fields for the Al 6061-O also overestimate the stress levels; however, the plastic zone shapes of the HRR seem to capture the general shape of this high strain hardening material.

Table 3.1: Initial crack length, critical load and J-integral

Test	a (mm)	P_c (N)	$J_{1_{DIC}}$ (kJ/m^2)	$J_{2_{DIC}}$ (kJ/m^2)	$J_{3_{DIC}}$ (kJ/m^2)	$J_{P-\Delta}$ (kJ/m^2)	J_{LEFM} (kJ/m^2)	Resol-ution $(\mu m/pixel)$
QSF-Al6061-T6-06	8.57	11,765	74.18	77.70	79.69	163.3	45.94	9.1
QSF-Al6061-T6-07	8.61	11,561	76.42	81.53	75.69	154	45.90	9.1
QSF-Al6061-O-04	8.96	4,046	114.1	114.7	115.9	161.2	6.10	8.2
QSF-Al6061-O-06	8.67	4,014	109.3	108.1	107.3	195	5.51	9.2

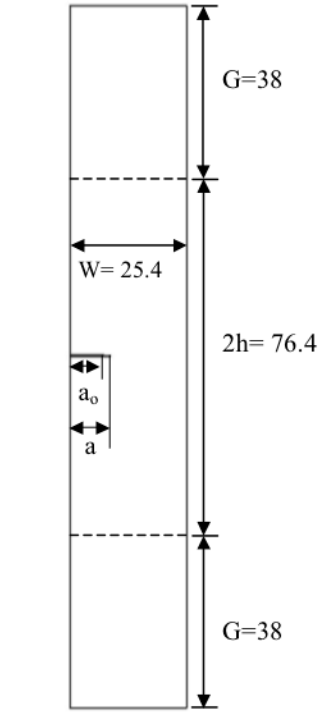

Figure 3.1a: Fracture specimen dimensions

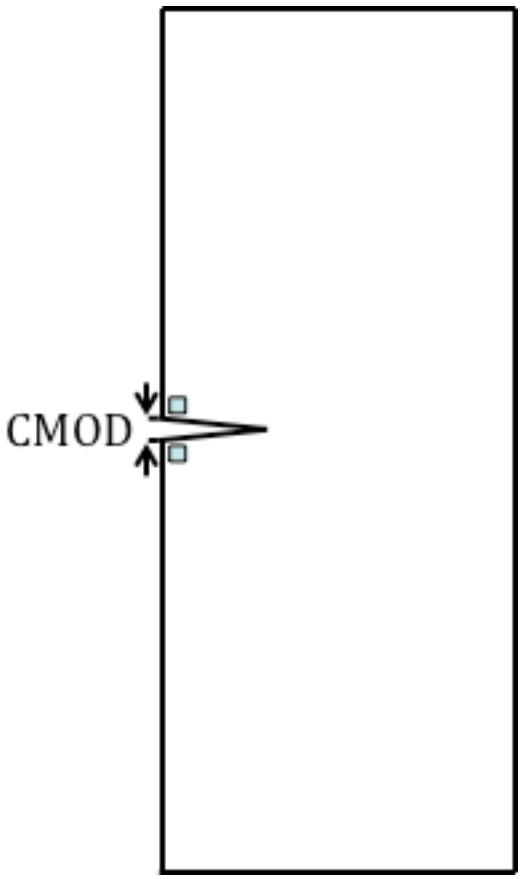

Figure 3.1b: Crack Mouth Opening Displacement

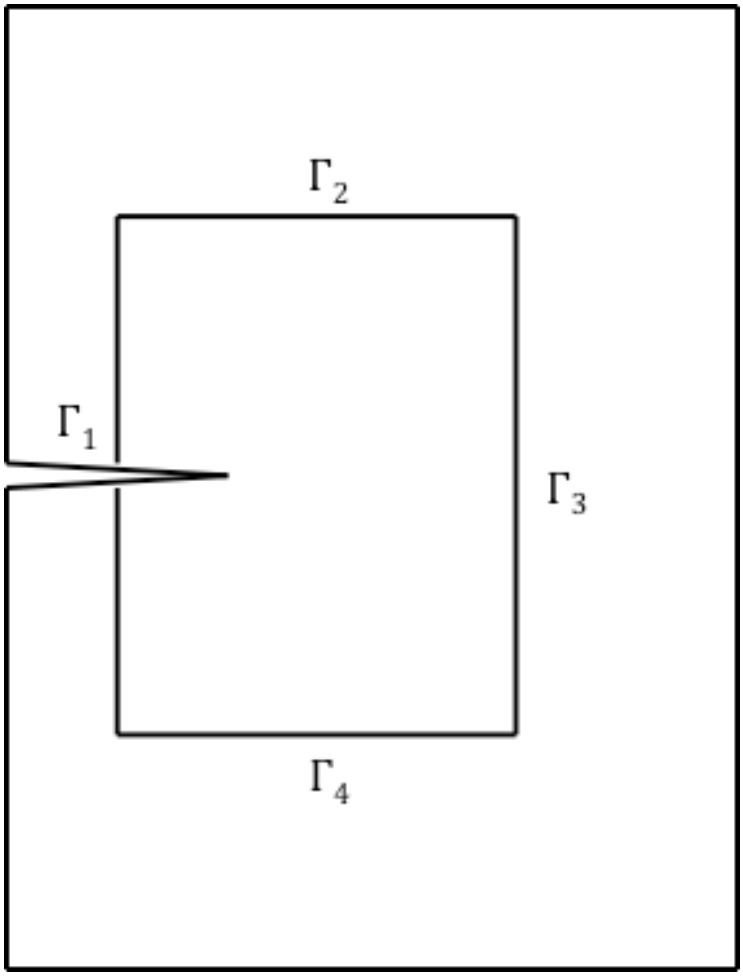

Figure 3.2: Example of contour used to calculate the J-integral as a line integral

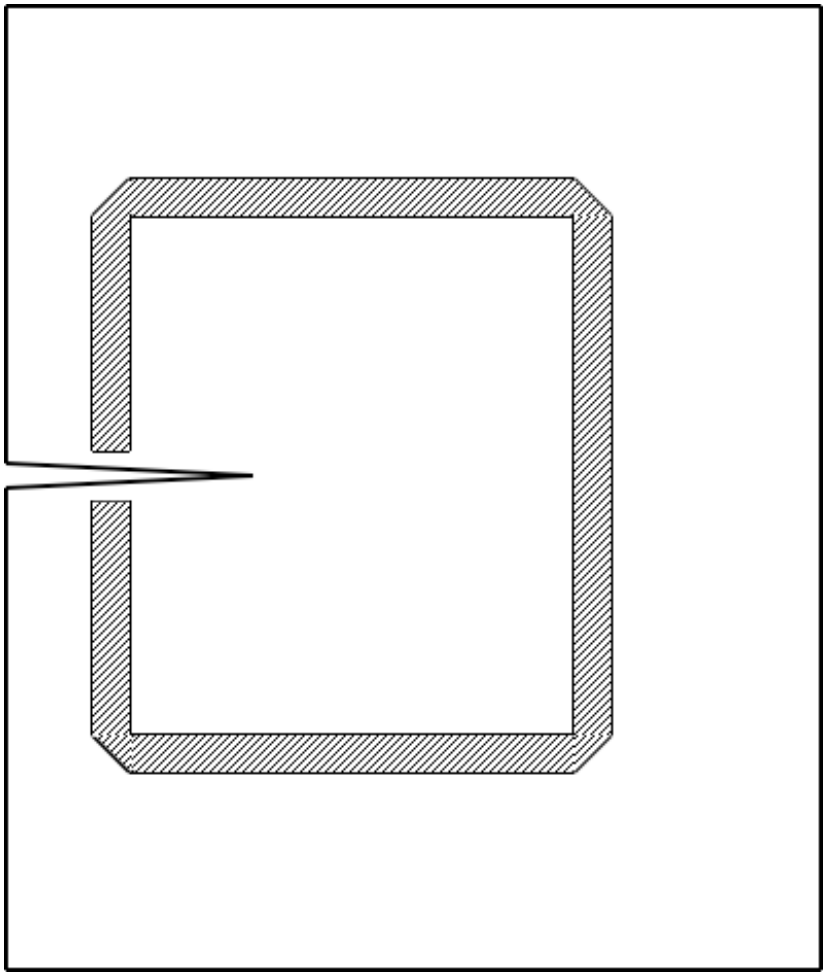

Figure 3.3: Example contours used for calculating the J-integral as an area integral

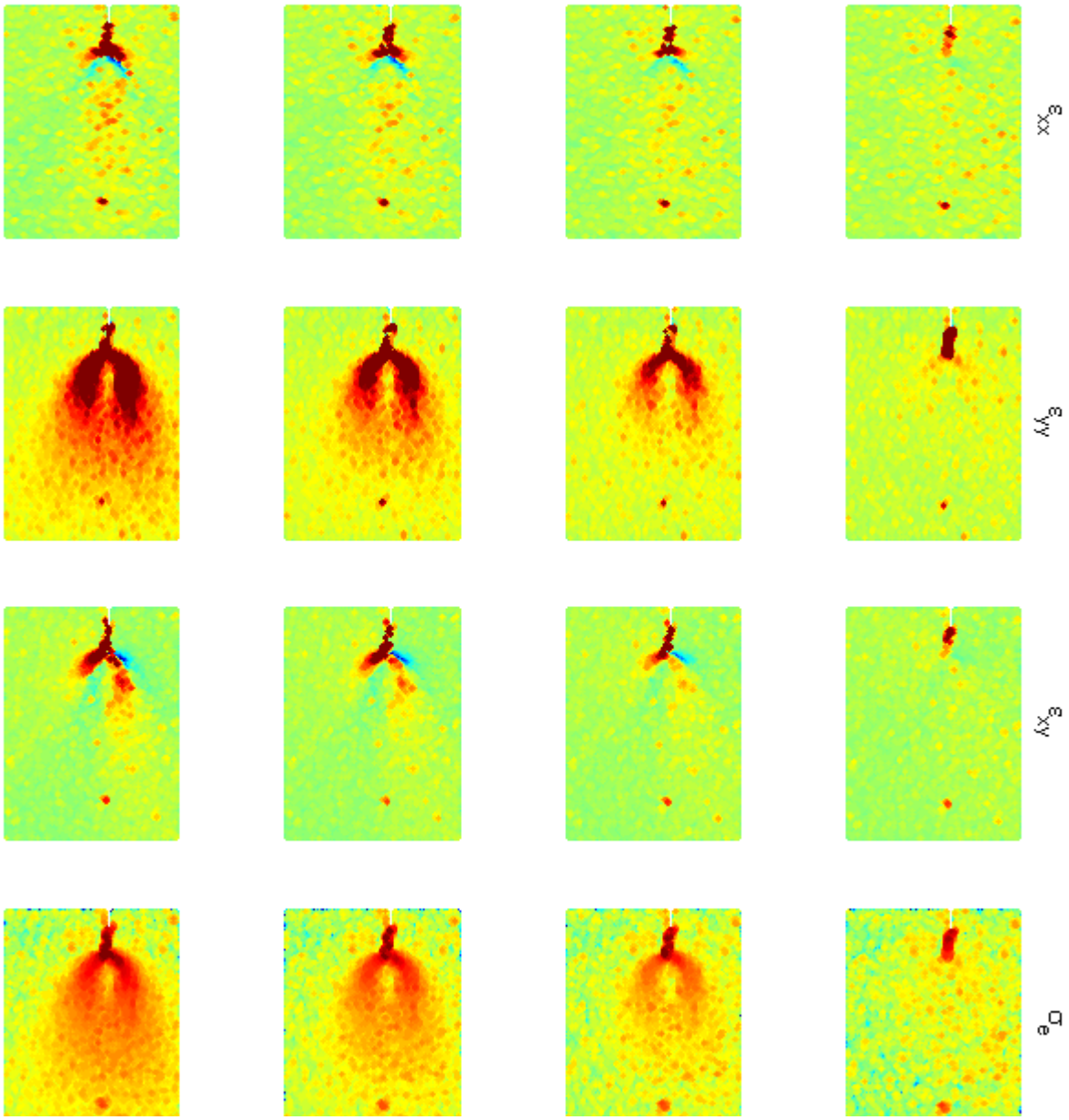

Figure 3.4: Contours of strain and equivalent stress of QSF-6061-T6-06

(for qualitative comparison)

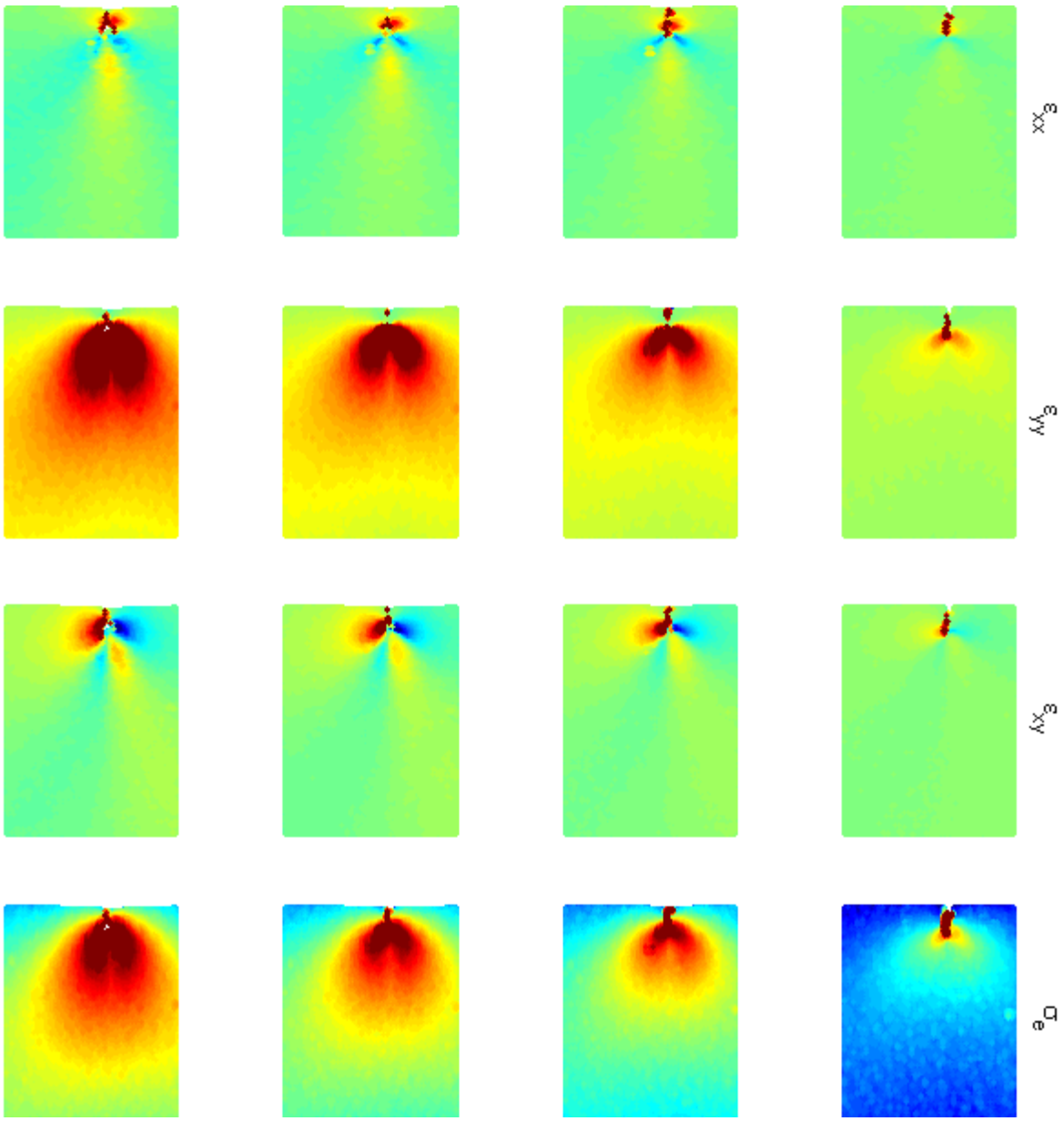

Figure 3.5: Contours of strain and equivalent stress of QSF-6061-O-06

(for qualitative comparison)

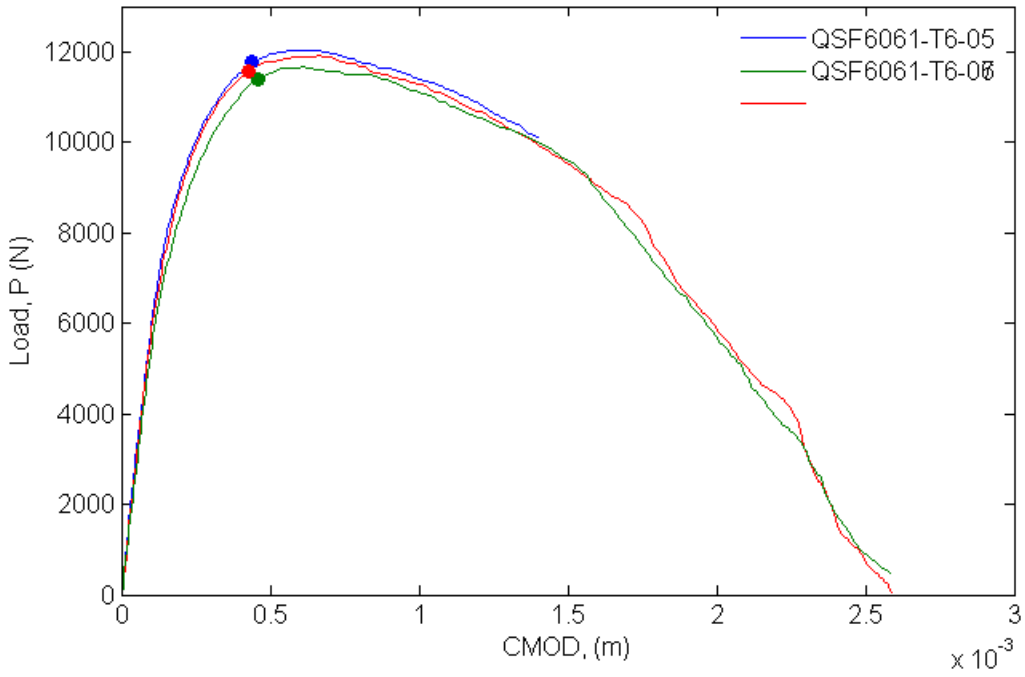

Figure 3.6: Load vs. CMOD for fracture tests of Al 6061-T6

(markers indicate crack initiation)

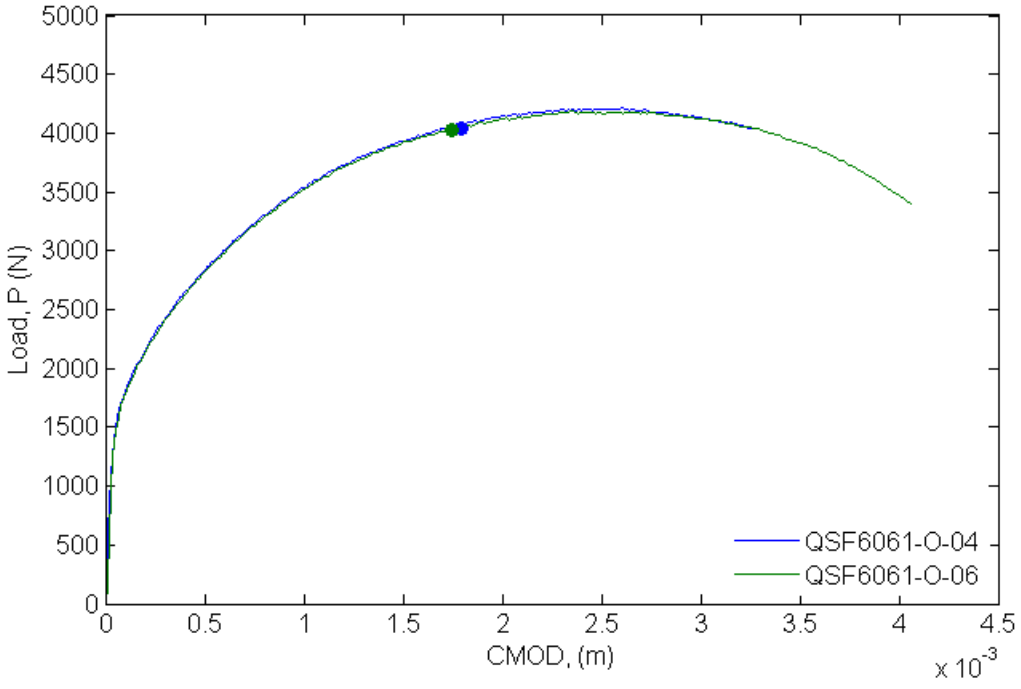

Figure 3.7: Load vs. CMOD for fracture tests of Al 6061-O

(markers indicate crack initiation)

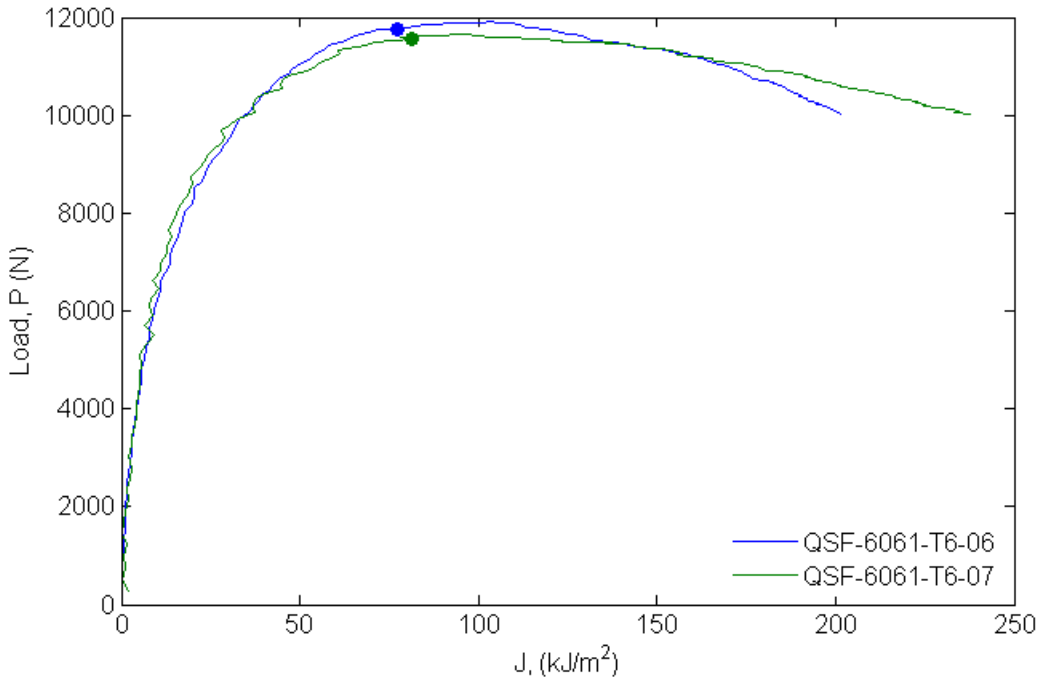

Figure 3.8: Comparison of Load vs. J for two different fracture tests of Al 6061-T6 (markers indicate crack initiation)

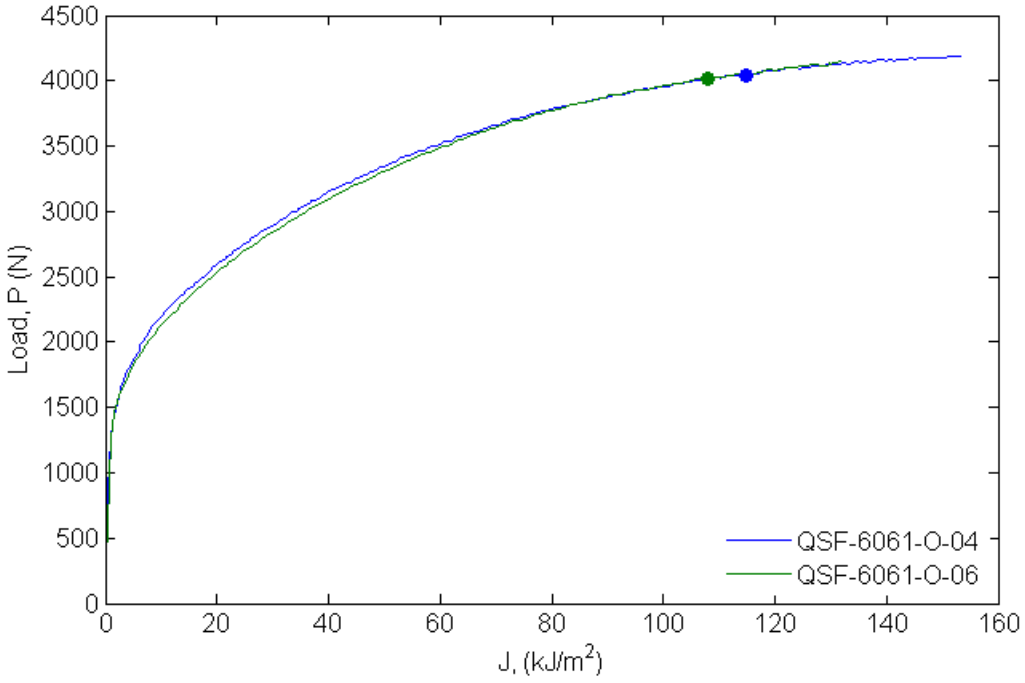

Figure 3.9: Comparison of Load vs. J for two different fracture tests of Al 6061-O (markers indicate crack initiation)

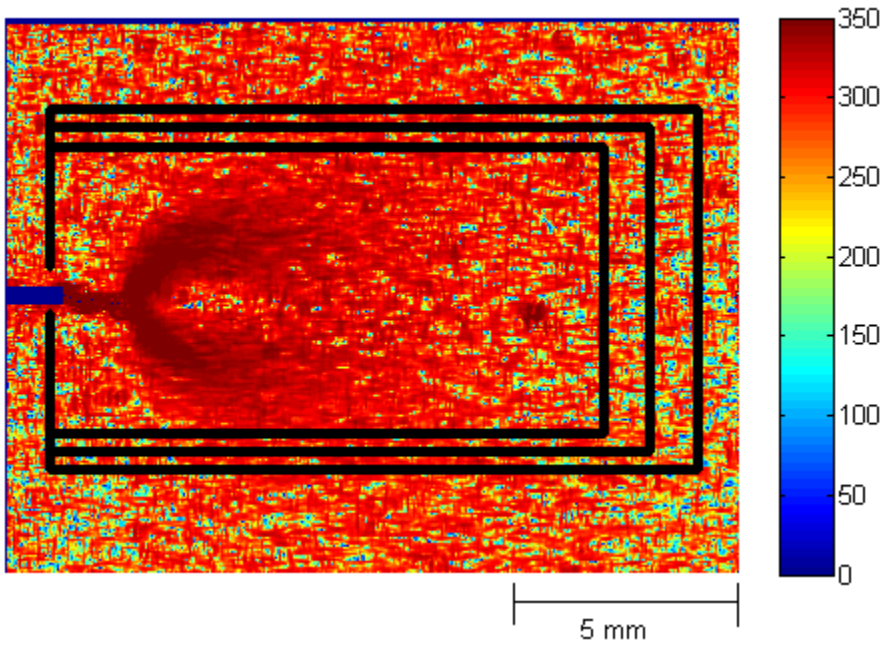

Figure 3.10: Contours used for calculation of J-integral of QSF-6061-T6-06 over equivalent stress contours

(colorbar in MPa)

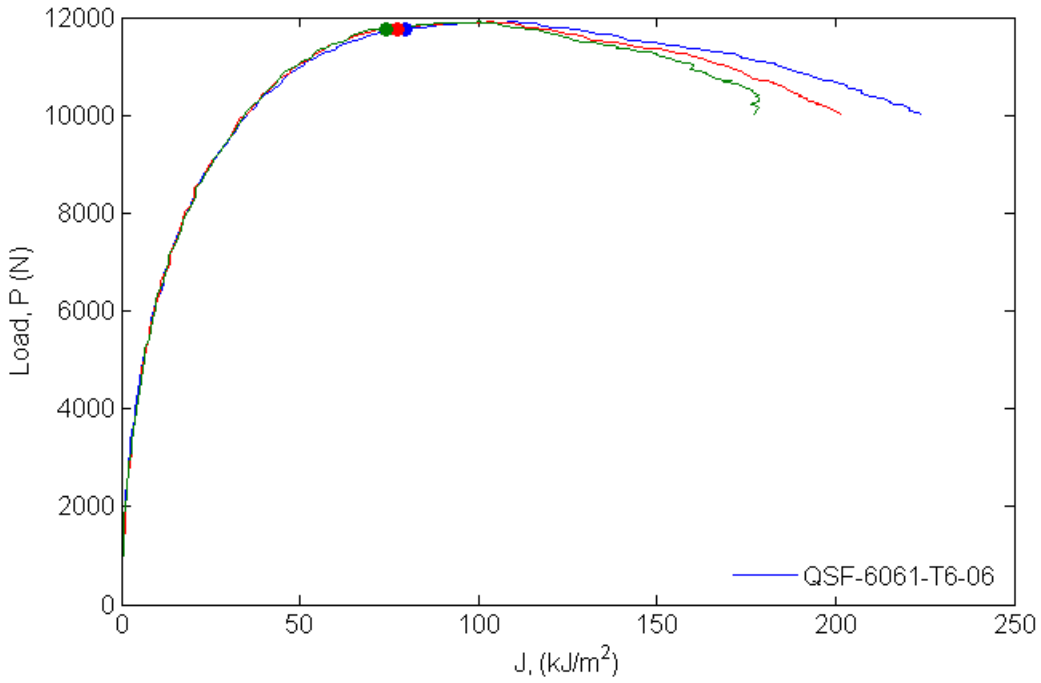

Figure 3.11: Load vs. J for three different contours of QSF-6061-T6-06

(markers indicate crack initiation)

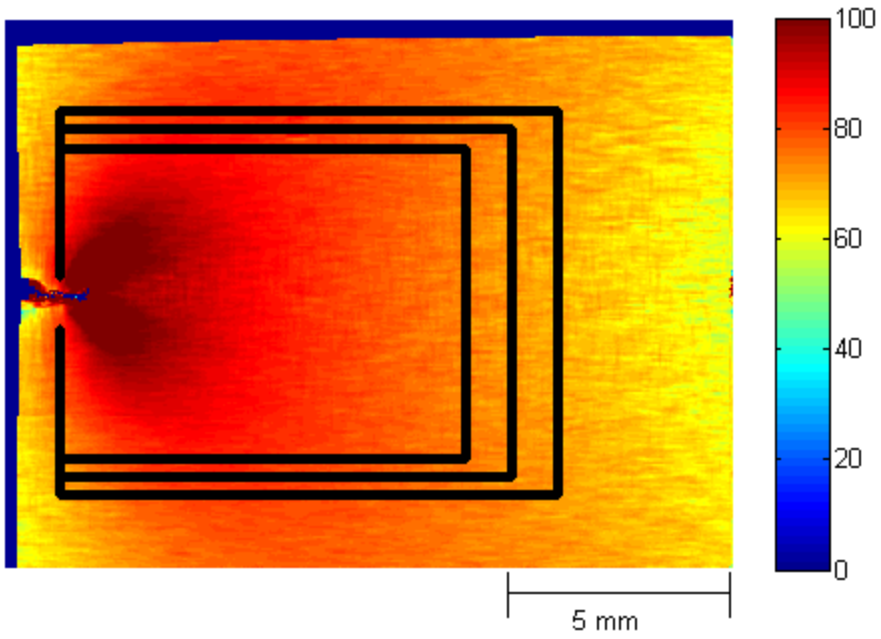

Figure 3.12: Contours used for calculation of J-integral of QSF-6061-O-04 over equivalent stress contours

(colorbar in MPa)

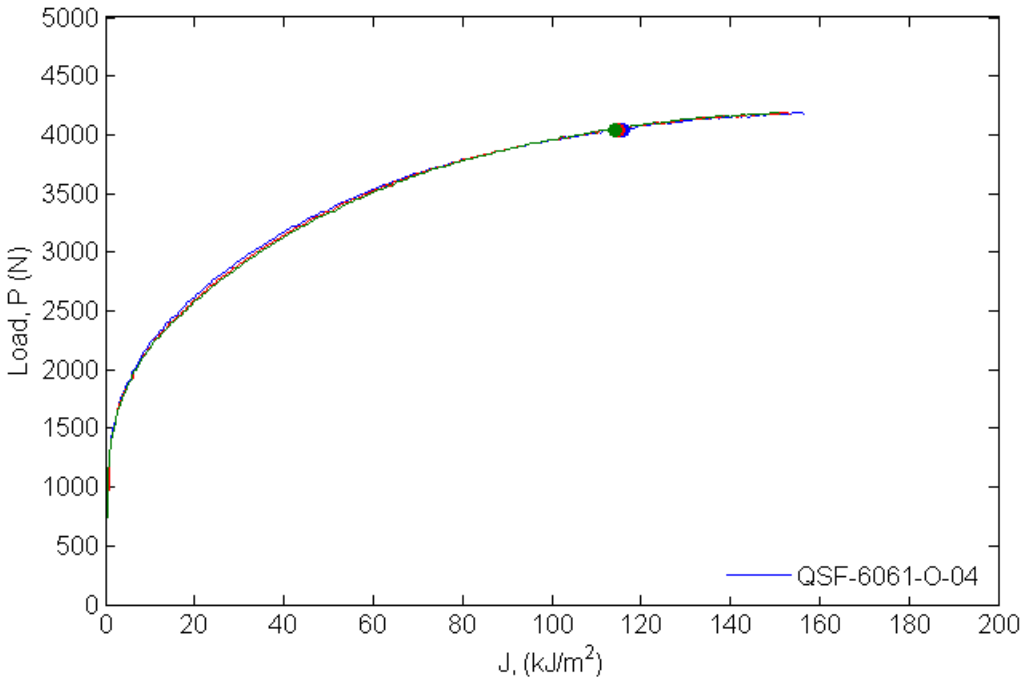

Figure 3.13: Load vs. J for three different contours of QSF-6061-O-04

(markers indicate crack initiation)

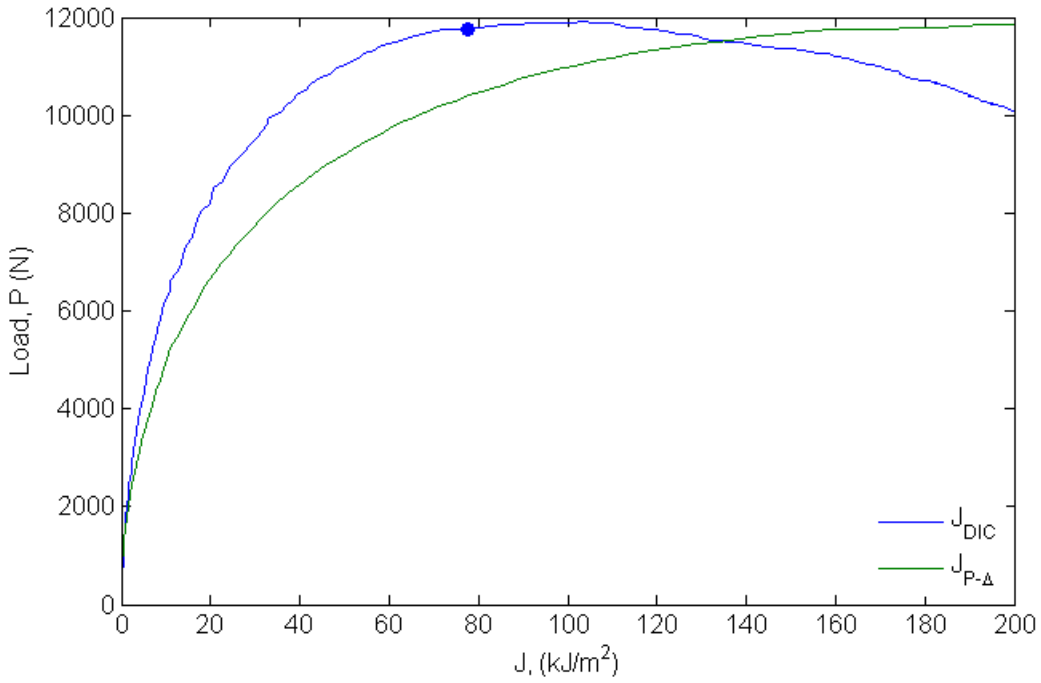

Figure 3.14: Load vs. J comparison for QSF-6061-T6-06 of DIC results and load-displacement calculation

(marker indicates crack initiation)

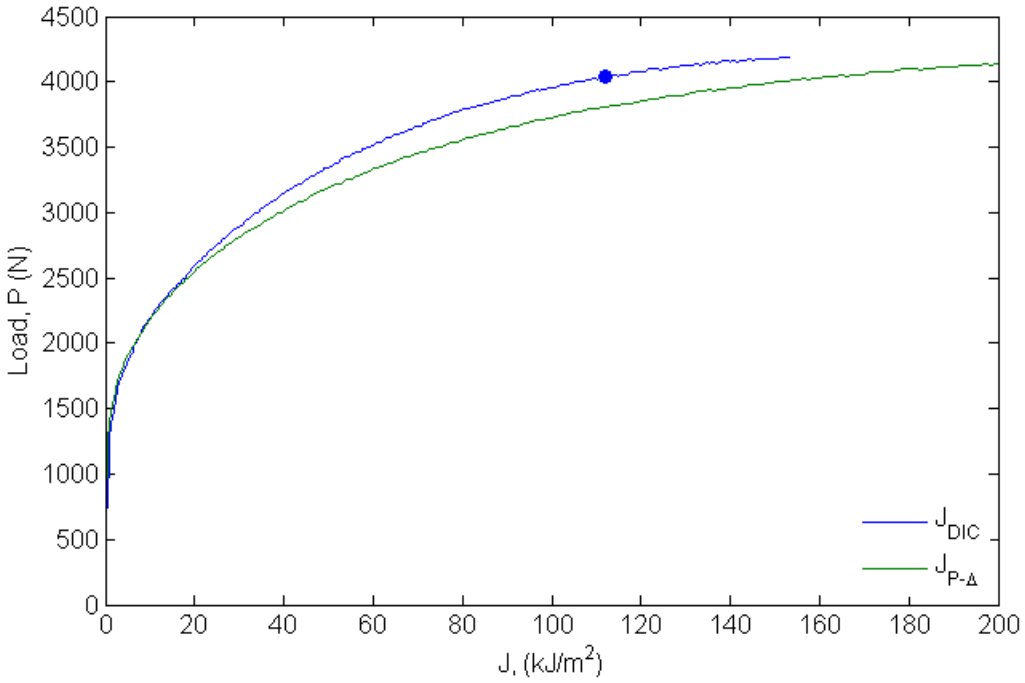

Figure 3.15: Load vs. J comparison for QSF-6061-O-04 of DIC results and load-displacement calculation

(marker indicates crack initiation)

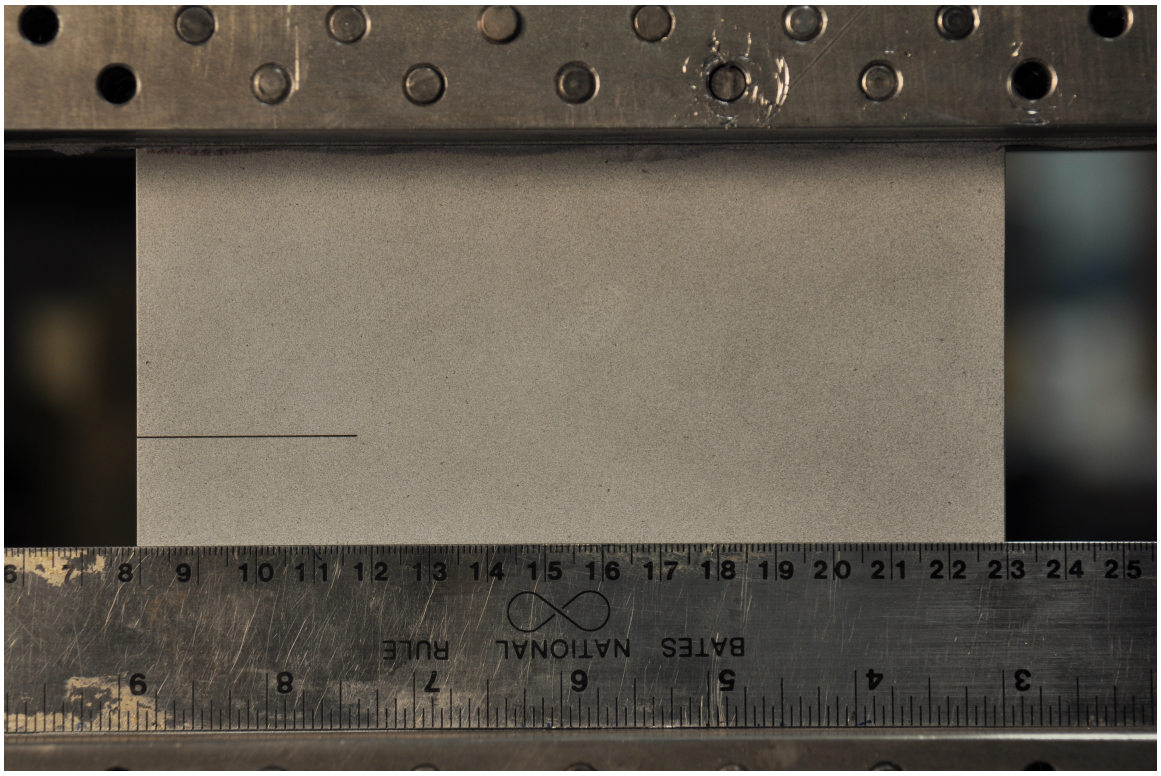

Figure 3.16: Large scale fracture test

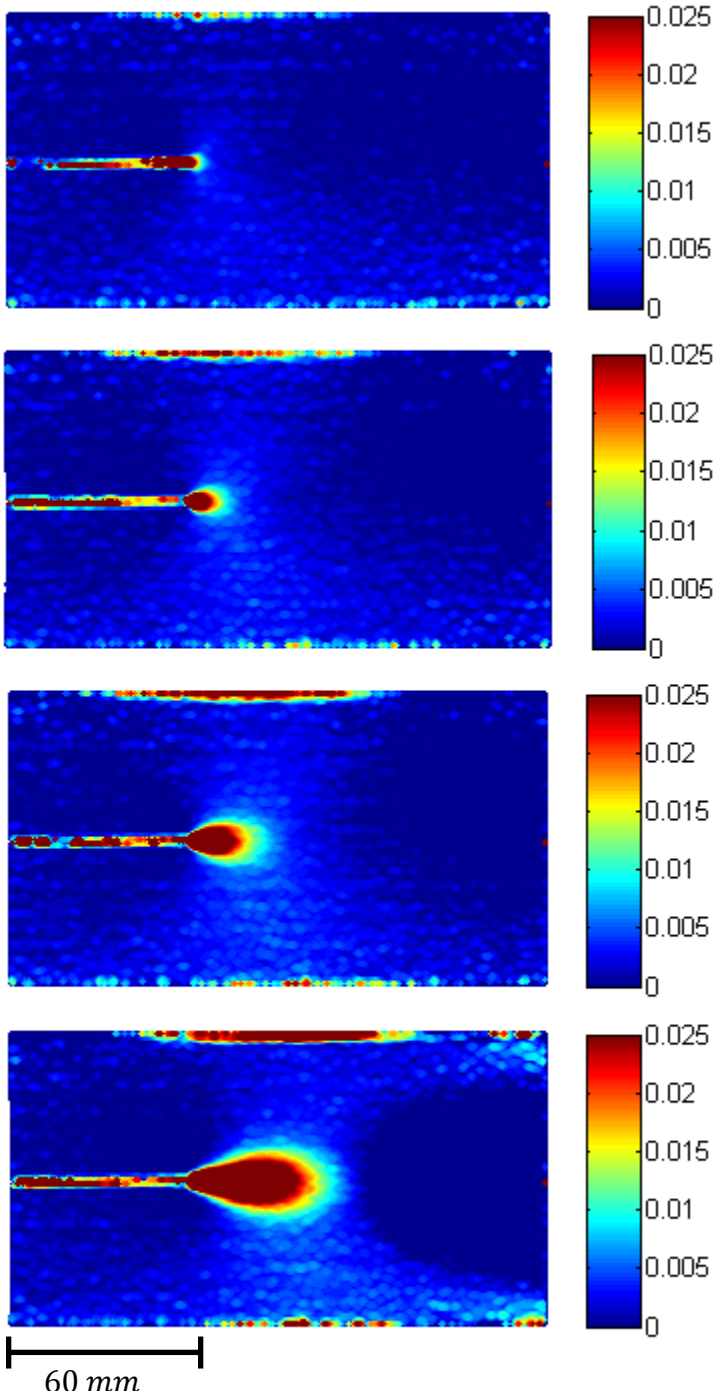

Figure 3.17: Evolution of major strain field for large scale fracture test

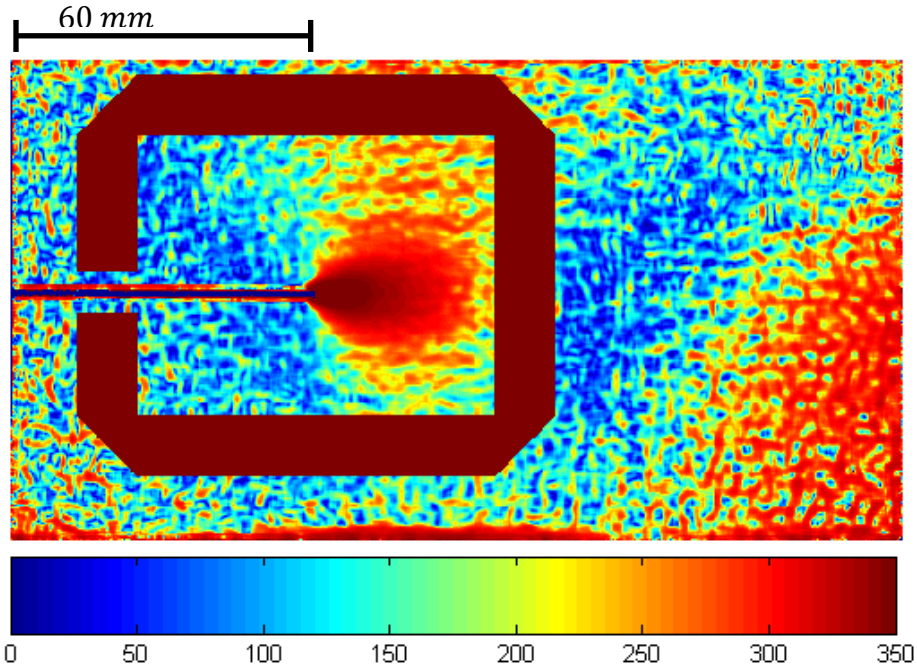

Figure 3.18: J-integral contour over equivalent stress field

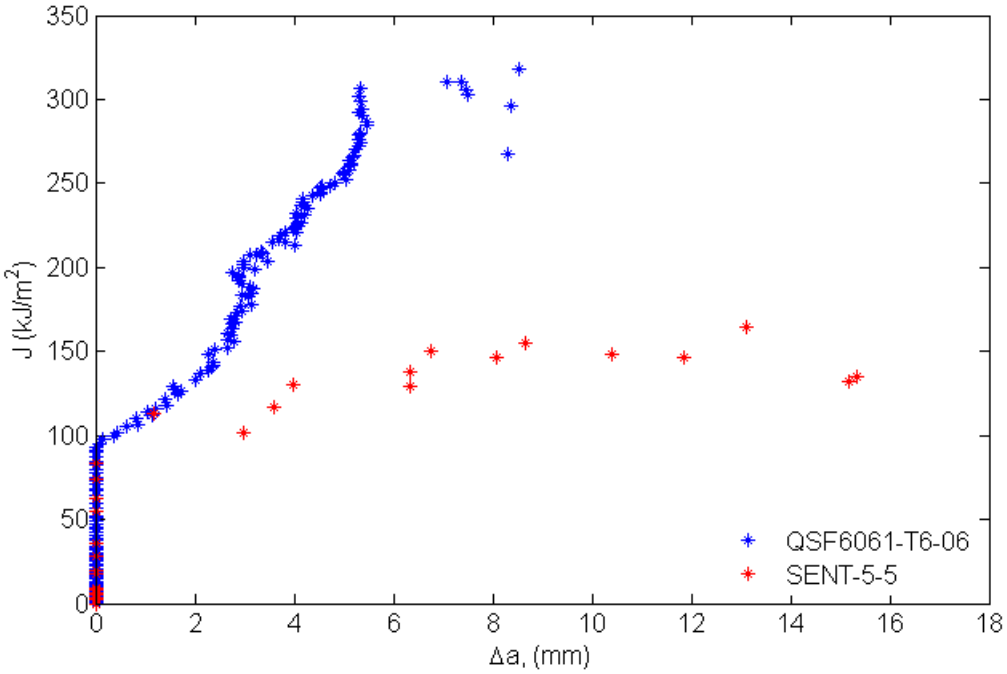

Figure 3.19: J-integral vs. change in crack length for SENT-5-5 and QSF6061-T6-06

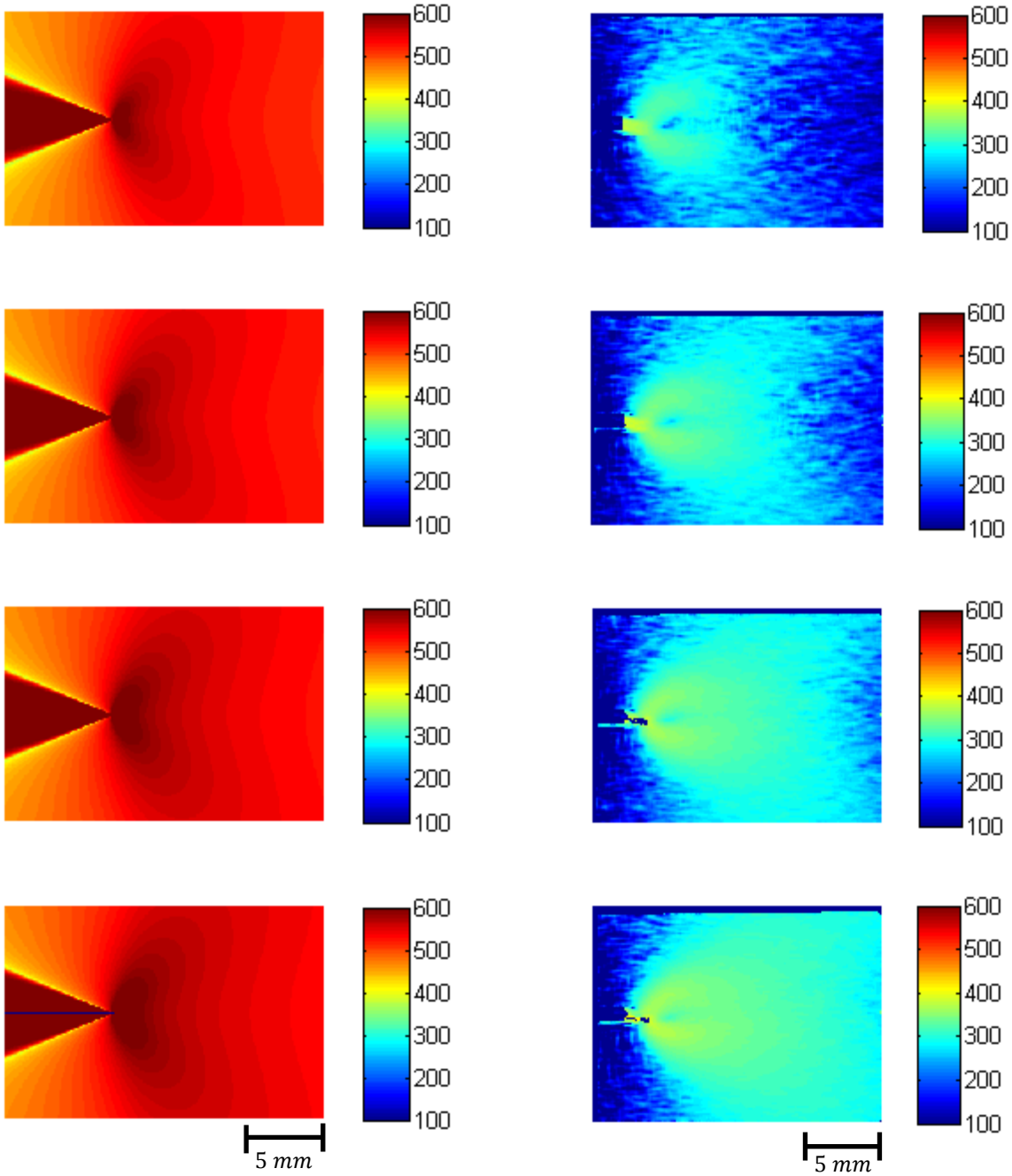

Figure 3.20: Equivalent stress contours for HRR field and experimental DIC data for Al 6061-T6

(colorbar in MPa)

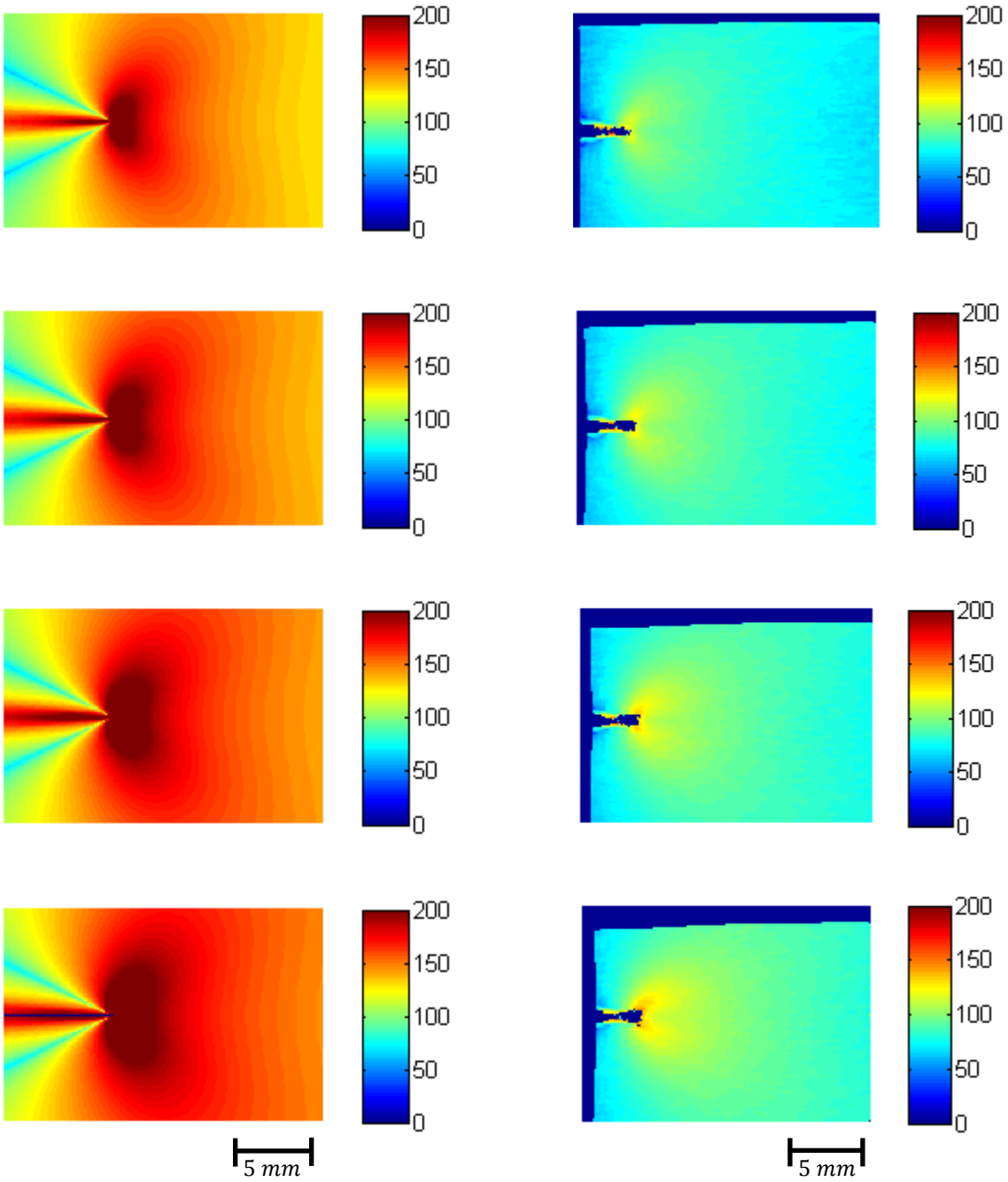

Figure 3.21: Equivalent stress contours for HRR field and experimental DIC data for Al 6061-O

(colorbar in MPa)

Chapter 4: Macroscopic and Microscopic Fracture Mechanisms

Macroscopic and microscopic observations of the fractured specimens help to understand fracture mechanisms involved during failure. Macroscopic observations will examine the plastic zone shapes, the plastic zone sizes and the angle of the fracture surface. Microscopic observations will include fracture surface features and grain level strain measurements.

4.1 Specimen Prepartation

For both microscopy methods, different sections of the fracture specimens were used. The fracture surfaces (nominally the *x*-*z* plane as shown in Figure 4.3) were observed in the SEM to identify the failure mechanisms. In addition, thickness sections of the specimens were cut to reveal the *y*-*z* plane. These pieces were then set into an epoxy resin and allowed to cure overnight. The specimens were then polished using a polishing wheel with different grit size silicon carbide papers, diamond compounds and colloidal suspensions. First, the specimens were polished with the silicon carbide abrasive discs on the polishing wheel lubricated with water for approximately one minute thirty seconds at three different levels: 240 grit, 600 grit and 1200 grit. Next, each specimen was polished in the same manner with both 3 μm and 1 μm diamond paste lubricated with oil. Finally, a 0.05 μm colloidal suspension was used to finish the procedure. When completed the specimens have a mirror like appearance. The polished specimens were also coated with approximately 50 nanometers of silver to ensure proper electric conduction between the specimen and the mounting holder in the electron microscope. The 6061 specimens can

also be etched to reveal the grains and grain boundaries; tracking the changes in the grain size provides an additional method of evaluating the local strains at the level of the grains and is pursued here. The specimens prepared for microscopy were etched, first in 2% aqueous solution of sodium hydroxide for about 55 seconds, and subsequently with Weck's (Weck and Leistner, 1986) alkaline solution (4% potassium permanganate + 1% sodium hydroxide) for about 15 seconds to obtain the contrast in the microstructure. This etching process allows excellent visibility of the grains and grain boundaries.

4.2 Macroscopic Observations

In these ductile alloys, the fracture surfaces for Mode I loading are either flat or slant relative to the thickness direction. In Al 6061-O, the fracture surface is macroscopically perpendicular to the loading direction; while in Al 6061-T6, the fracture surface is at approximately a 45-degree angle with the loading direction. Both slant and flat fracture are displayed in Figures 4.2 and 4.3. It is also important to recognize from these figures that the average strain in the thickness direction is significantly greater in the case of flat fracture. For the slant fracture, the thickness direction strain is ~0.16 while the flat fracture experiences a thickness strain of ~0.85.

Slant fracture is not fully understood and various explanations have been proposed. The classic textbook example is that flat fracture usually arises when plane strain conditions prevail during which the crack-tip is in a triaxial state of stress, and void growth and coalescence occurs in the areas of maximum stress triaxiality. In thin plates, plane stress conditions prevail and the maximum shear stress is oriented at 45° from the

free surface. This explanation is unsatisfactory or incomplete, since both materials used in the present work used the same thickness specimens with similar development of plane stress conditions.

For thin aluminum sheets with low strain hardening, the flat and slant fracture patterns have been attributed to loading in the different directions relative to the rolling direction (See Rosakis, et al 1998). However, in the tests reported here, the rolling direction did not have any effect on the type of fracture. For the Al 6061-T6, slant fracture occurred when the crack was oriented either in the rolling direction or transverse to the rolling direction.

The development of initial fatigue crack and the local measurements of the strain field during monotonic loading clearly indicate that the mode of cracking – flat vs. slant – is influenced by the stress state that develops in front of the crack tip, which in turn is influenced by the strain-hardening behavior and plastic response of the material. We resolve the issue through the following observations:

- The strain fields measured with DIC easily allow for visualization and quantitative characterization of the development of the plastic zone in the two different materials. Large differences in the development of the plastic zones for Al 6061-T6 and Al 6061-O are shown in Figure 4.4. In the Al 6061-O (right column of Figure 4.4), the plastic zone shape resembles that calculated using the plane-strain K-field and imposing a von Mises yield criterion. Very large strains – as large as 0.1 – are generated at distances of about 5 mm from the crack tip; this results in a significant thinning of the plate as well as seen

Figure 4.3. The high strain-hardening exponent ($n = 0.22$) of the material implies that deformation instabilities in the form of localization do not occur until strain levels are extremely large (for example, necking instabilities could be triggered in sheets under uniform plane strain deformation at a strain level $\sim 2n$). A high triaxial stress state is developed along $\theta = 0$, triggering ductile fracture failure processes along this direction and resulting in a flat fracture surface.

- In contrast to this behavior, the plastic zone shape in Al 6061-T6 bears no resemblance to estimates based on either the plane strain or the plane stress K-field! (See Figure 4.4 left column) In fact, along $\theta = 0$, the strains are extremely small and remain in the elastic state, quite contrary to the expectations of plane stress! The aging heat-treatment of T6 increases the yield strength significantly in comparison to the annealed material, but the strain-hardening exponent is decreased significantly. As indicated in Chapter 2, n is approximately 0.058 for Al 6061-T6; therefore, localization of deformation could be expected at low strain levels, and this is only exacerbated in the vicinity of the crack tip. Therefore, with increasing global load, the deformation in Al 6061-T6 localizes along planes that are oriented at $\pm 45°$ with respect to the normal to the crack surface (or the sheet surface); the visible traces of the large deformations within this band on the free surfaces can be identified in the strain fields obtained from DIC. Once such localization occurs, deformation outside this plane ceases, and ductile failure processes could occur

only within this plane. This results in a slant fracture surface, as well as very little thinning deformation of the sheet outside this plane (see Figure 4.2).

- Low magnification scanning electron micrographs of the fracture surfaces of the two different heat treatments are shown in Figure 4.5 and 4.6. The initial fatigue precrack surface – which was created with a stress intensity level of $22\ MPa\sqrt{m}$ in the T6 and $17\ MPa\sqrt{m}$ in the O (equivalent J at 0.092 of J_c for T6 and 0.045 for O) – is flat for both materials. At this low loading condition, the plastic zone size can be estimated to be $\sim 870\ \mu m$ for the T6 and $\sim 20\ mm$ for the O. Since plasticity is confined to a fraction of the overall specimen thickness ($2.438\ mm$) in the T6, localization of deformation as discussed above cannot appear in the Al 6061-T6, and therefore the fatigue crack grows as a flat fracture in both materials.

Combining these observations, one can generate a mechanistic understanding of flat and slant fracture in sheet metals. At low loading levels, such as those during fatigue crack growth, plane strain conditions exist near the crack tip even in thin sheet metals. Under this condition, the ductile failure process (irreversible slip etc) are triggered along the plane $y = 0$, and results in a flat fracture surface. During crack growth under monotonic loading, the deformation is critically dependent on the strain-hardening exponent, since stability of deformation depends on this parameter. For materials with high strain-hardening, localization instabilities do not appear until very large strain levels and therefore the diffuse plastic field dictated by the crack tip stress concentration (K-field or HRR type) is generated; the resulting high triaxiality along $\theta = 0$ triggers ductile failure

processes resulting in a macroscopically flat fracture surface. On the other hand, for materials with a low strain-hardening exponent, plastic instabilities arise at extremely low strain levels and localize deformation along two equivalent slant planes. Further straining and damage occur only within these zones.

4.3 MICROSCOPIC OBSERVATIONS

Both optical microscopy and scanning electron microscopy were utilized to further characterize the fracture process of Al 6061-T6 and Al 6061-O. The examination of different planes and surfaces of the post-mortem fracture specimens provides insight into the failure mechanisms. Initial examination of the fracture surface indicates the type of fracture exhibited by the materials.

4.3.1 Fracture Surface Observations

In ductile materials, the material undergoes large plastic deformation in front of the crack tip, and under these conditions, failure is classically thought to occur from void growth and coalescence. Low magnification scanning electron micrographs of the fracture surface of the Al 6061-O and Al 6061-T6 are shown in Figures 4.5 and 4.6, respectively. Two distinct regions are present on the fracture surfaces of both alloys. The surface of the fatigue crack region is smooth with no dimples (seen above left in both Figures 4.5 and 4.6), and the surface of fracture consists of many dimples as shown in the high-magnification images of both alloys shown in the top right of both figures.

As can be seen in these fractographs, many small dimples are present on the fracture surfaces of both the Al 6061-O and Al 6061-T6. In the Al 6061-O, the dimples

appear to be two distinct sizes. The Al 6061-T6 fracture surface dimples also appear in two sizes, but the smaller dimples are smaller and the larger dimples are larger than the Al 6061-O. These dimples are typically taken to be evidence of ductile failure by void nucleation, growth and coalescence with the void nucleation occurring preferentially at the sites of the second phase particles; examination of the fractographs at high resolution shows the presence of such void nucleating particles in each large dimple of the fracture surface.

4.3.2 Cross-sectional Observations

In order to examine the details of the progression of the void nucleation, growth and coalescence, loading of the specimens was halted before complete failure. The cracks usually tunnel deeper in the central portion of the thickness than towards the plate free surfaces. One specimen each of Al 6061-O and Al 6061-T6 was interrupted in this manner and then prepared for observation: the specimens were cut to reveal the *y*-*z* plane, at an *x*-location where the tunneling crack is intersected. These specimens were mounted in epoxy and polished for microscopic examination. Scanning electron micrographs of the tunneling cracks are shown in Figures 4.7 and 4.8 for the Al 6061-T6 and Al 6061-O, respectively. The following important observations can be made from these images.

- The SEM images indicate a number of white particles distributed over the image; these have been identified through EDAX to be iron particles that are added during manufacturing of the alloy. They are typically elongated particles, with the small

dimension being around a couple of μm, and the longer dimension $\sim 5\,\mu m$. The total volume fraction of such particles is in the range of 1%.

- For the Al 6061-T6, the overall orientation of the fracture plane is at $\pm 45°$ with respect to the loading direction; the crack opening is seen to be extremely small; it is not easy to identify the position of this slice relative to the crack tip, but the overall crack opening is in the range of $3\,\mu m$. For the Al 6061-O, the overall orientation is perpendicular to the loading direction, but it appears to be made of alternating segments oriented at $\pm 45°$.
- Many of the second phase particles have broken into fragments in the Al 6061-T6 (see high magnification inset image in Figure 4.7); there is also some debonding or growth of the void associated with the particle. However, the Al 6061-O shows almost no breakage of the second phase particles and no voids; since the yield strength of this material is so much lower, the material probably flows around the particles rather than develop a high stress in them.
- In both materials, fracture appears through the nucleation of damage at the second phase particles and then subsequently by the connections established between the nuclei; there appears to be very little damage outside of a small neighborhood of the fracture plane. Compared to the number of dimples that are seen in the fracture plane, damage in the form of nucleation (by debonding or fragmentation of second phase particles) and growth of cavities by plastic flow around the cavities appears to be negligible. From careful examination of the images in Figures 4.2 and 4.3, the

region in which there is any damage at all in the T6 material can be estimated to be around $\sim 150\ \mu m$, and in the O material there exists no discernable damage.

4.3.3 Quantitative Microscopy and Grain Based Strain Measurements

The DIC images shown in Figure 4.4 indicate that the strains near the vicinity of the crack are indeed quite large. However, this method decorrelates in the vicinity of the crack tip for two important reasons: first, the strains are quite large and an extreme distortion of the images arises; second, the large out-of-plane displacements near the crack cause image degradation also leading to decorrelation. On the other hand, the etched thickness section images shown in Figures 4.2 and 4.3 permit evaluation of thickness-averaged strains that are in the range of 0.16 for the T6 and 0.84 for the O.

The local values of strain are estimated using the following procedure: first, the distribution of grain size in the initial microstructure was estimated from the images of the unstrained microstructure; this distribution is shown in Figure 4.9, yielding an average grain size of $15.1\ \mu m$ and the standard deviation of $6.6\ \mu m$. Next, the deformated grain images were examined quantitatively: an example of a *y*-*z* section of a fracture specimen is shown in Figure 4.10; a magnification view of the crack tip region is shown on the right side of this figure. This specimen corresponds to a slant fracture in Al 6061-T6. The location of each grain boundary was identified visually along the green horizontal lines marked in Figure 4.10, corresponding to different depths below the fracture plane and captured into a data file using a MATLAB code. The variation of the grain width t across a few lines $y =$ constant was obtained, and divided by the mean

grain width $\hat{T}$ in the *y-z* plane to obtain an estimate of the strain in the thickness direction $\varepsilon_t = \ln(t/\hat{T})$. Then the equivalent plastic strain can be estimated assuming plastic incompressibility: $\varepsilon_{eq} = \frac{2}{\sqrt{3}}\ln(\hat{T}/t)$. Estimates for the thickness strains are shown in Figure 4.11. These strains were calculated from the grain widths along the green lines shown in Figure 4.9. The red-dashed lines in Figure 4.11 indicate the average strain measured in the cross section. The average grain level strain measurements appear to be similar to the macroscopic strains measured, but the local maxima are significantly greater.

Very large grain rotations (macroscale shear) and grain elongations can be observed very close to the fracture plane; grain measurements were made just below the fracture surfaces in both the T6 and O materials. For the T6 material, the grain level thickness failure strain close to the fracture plane was 0.67; this is a significant increase from the macroscopic thickness failure strain of 0.51 measured in the quasi-static tension tests. The annealed material exhibited a grain level thickness failure strain of 1.06, and a macroscopic thickness failure strain of 0.75 in the quasi-static tension tests.

The large difference in the macroscopic and grain level failure strains for these materials has noteworthy implications in the modeling of failure and fracture. If the large-scale strains are used as failure strains in simulations, the failure will be made to occur prematurely, thus greatly distorting the evolution of the stress and strain fields.

This result also calls into question failure strains estimated through finite element simulations. Typically these studies involve matching a load displacement curve of the

simulation with that of an experiment (see Wierzbicki, et al 2004), identifying the failure location within the specimen, finding the corresponding location in the model and evaluating the equivalent plastic strain at failure load-displacement. Without careful observations of the localizations, this can lead to deceptive results. As demonstrated in Figure 4.4, the development of the localization in the T6 and O materials are very different. Without these DIC and grain based observations, the load-displacement response for the slant fracture could be matched with flat fracture and a failure strain approximated.

The failure in the low strain-hardening material is an extremely localized event. Support for this conclusion can be obtained from Figures 4.9 and 4.11. On the lowest green line on the fracture specimen of Figure 4.9, the average strain level is approximately 0.4. This line is very close to the fracture surface; however, the strains observed on the fracture surface are greater than 0.67! Similarly, the large increase in grain level strain for the annealed material is also localized. Due to the nature of localization, the mesh size necessary to determine failure strains must be on the order of the average grain size.

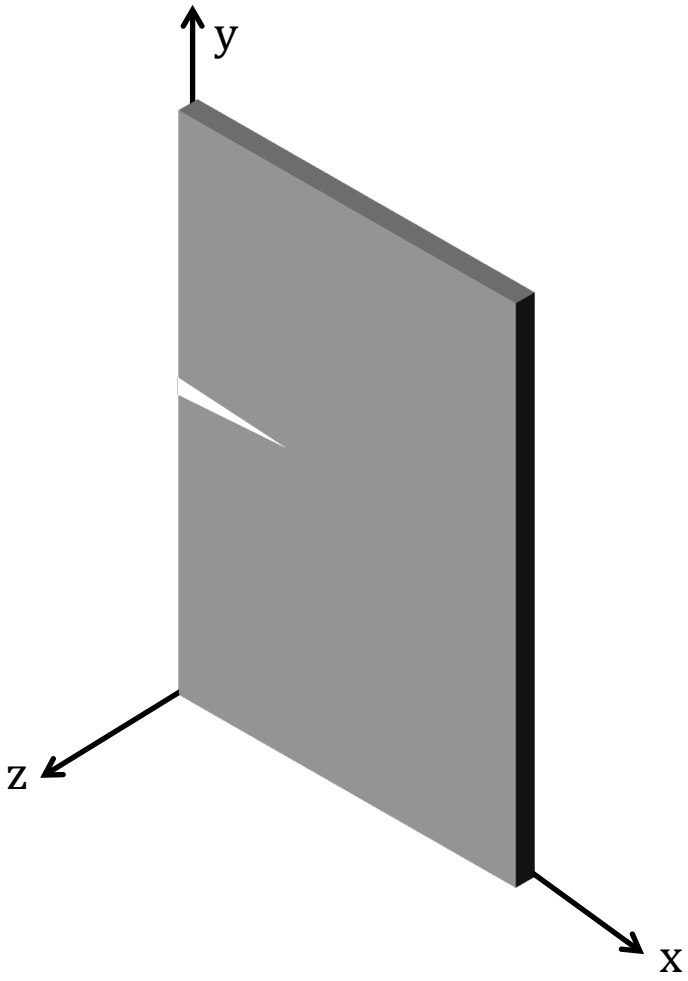

Figure 4.1: Plane orientations with respect to the specimen

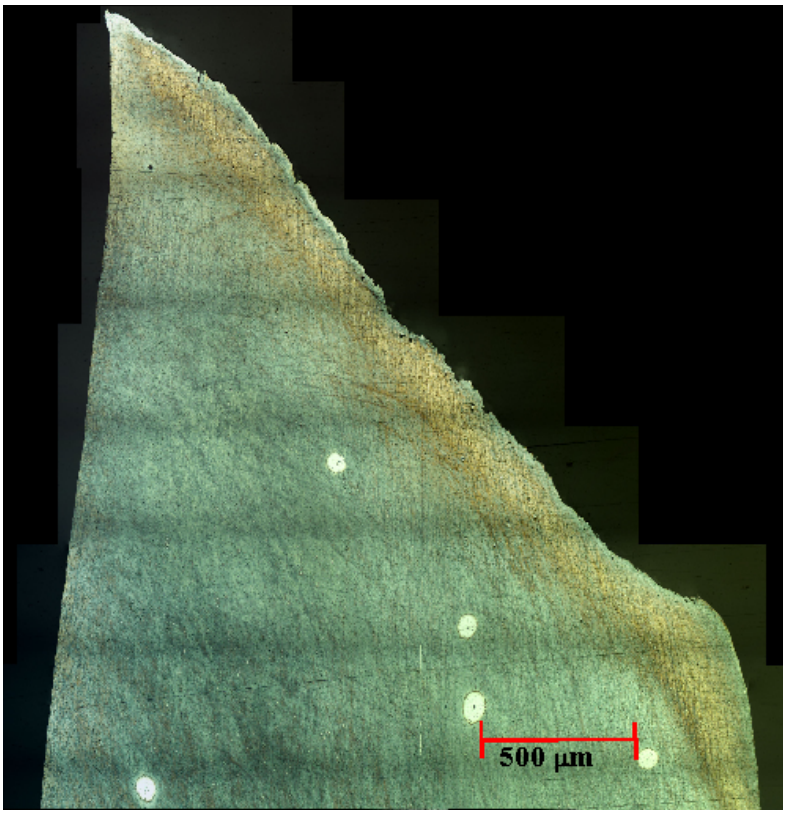

Figure 4.2: Slant fracture in Al 6061-T6

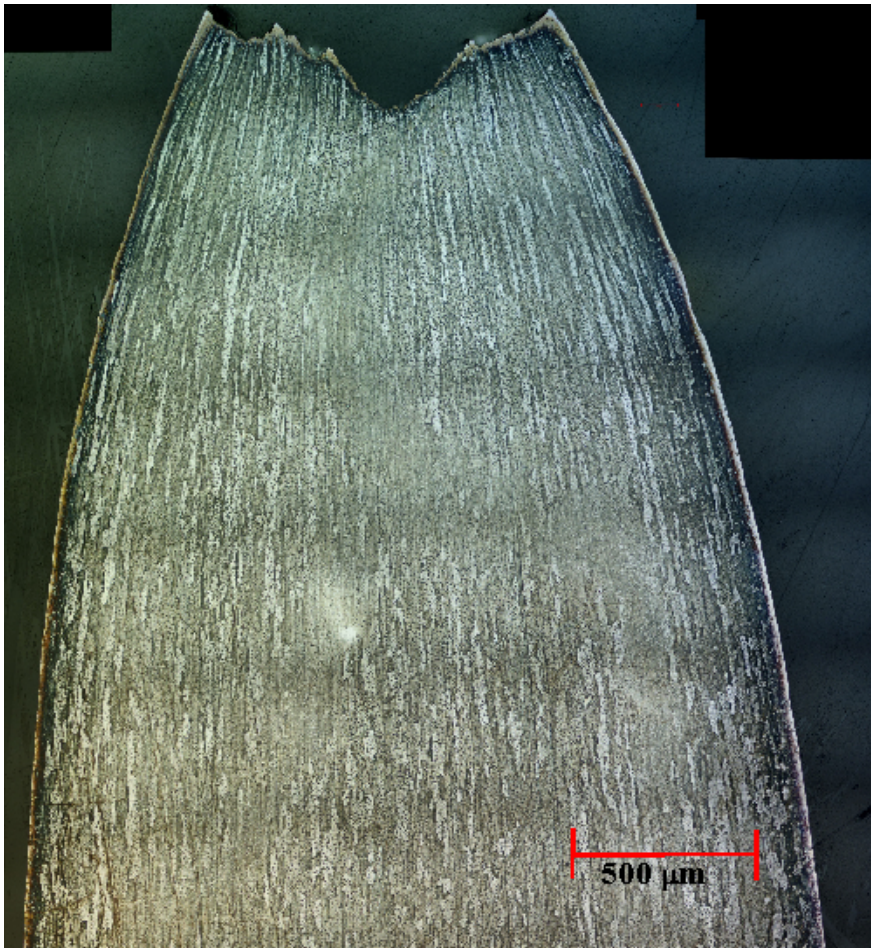

Figure 4.3: Flat fracture in Al 6061-O

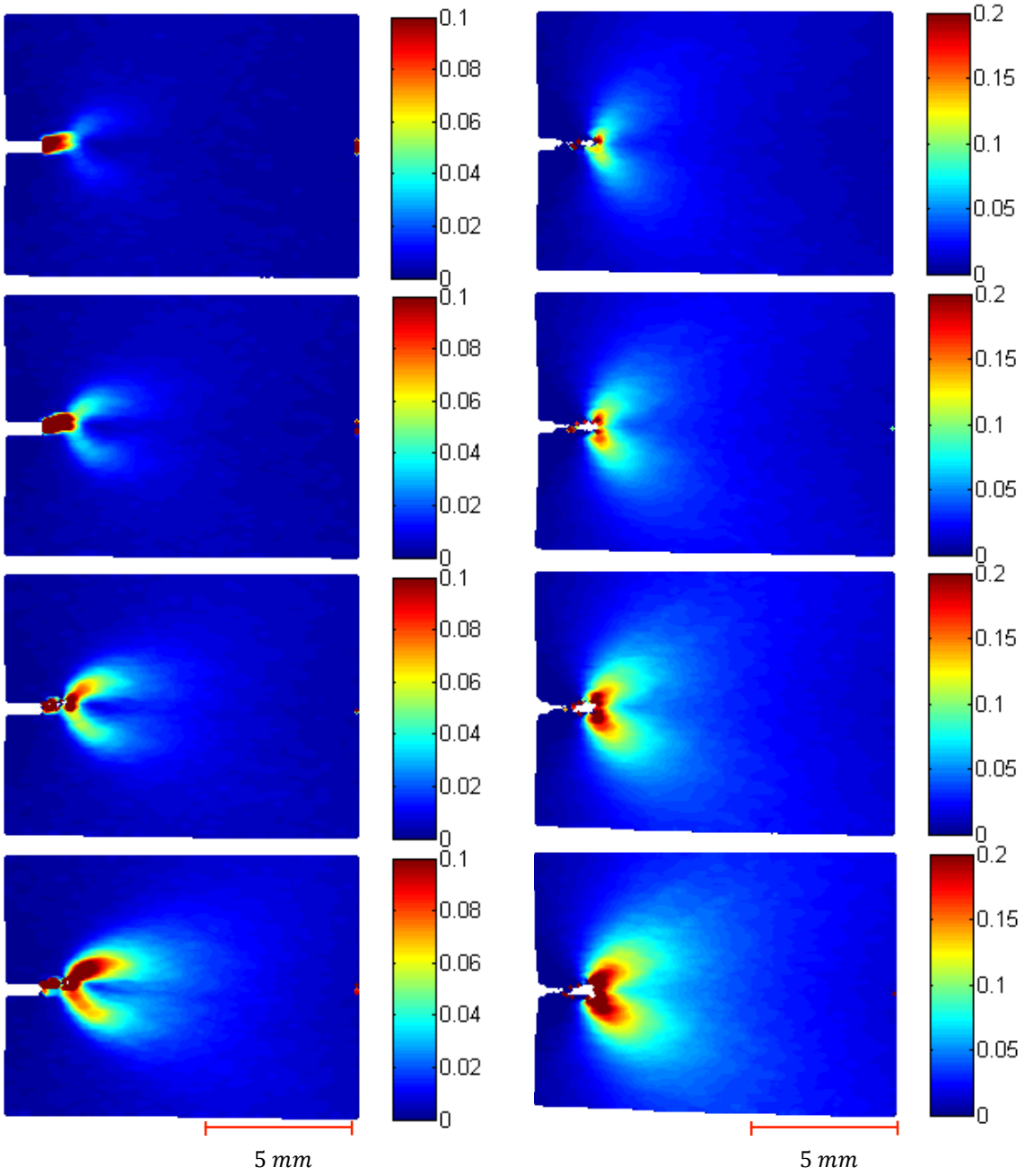

Figure 4.4: Comparison of major strain fields

Al 6061-T6 on left and Al 6061-O on Right

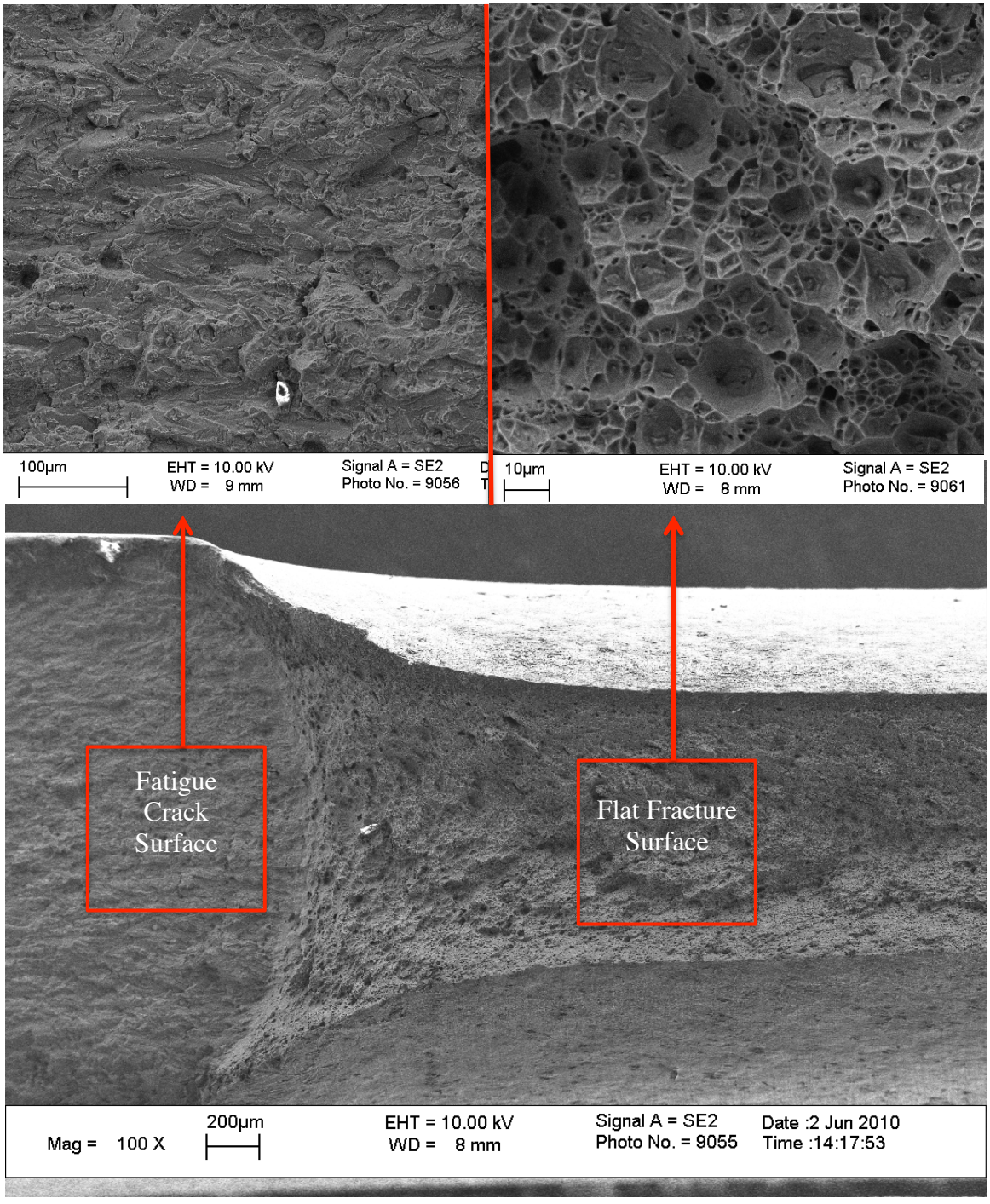

Figure 4.5: Fracture surface of Al 6061-O

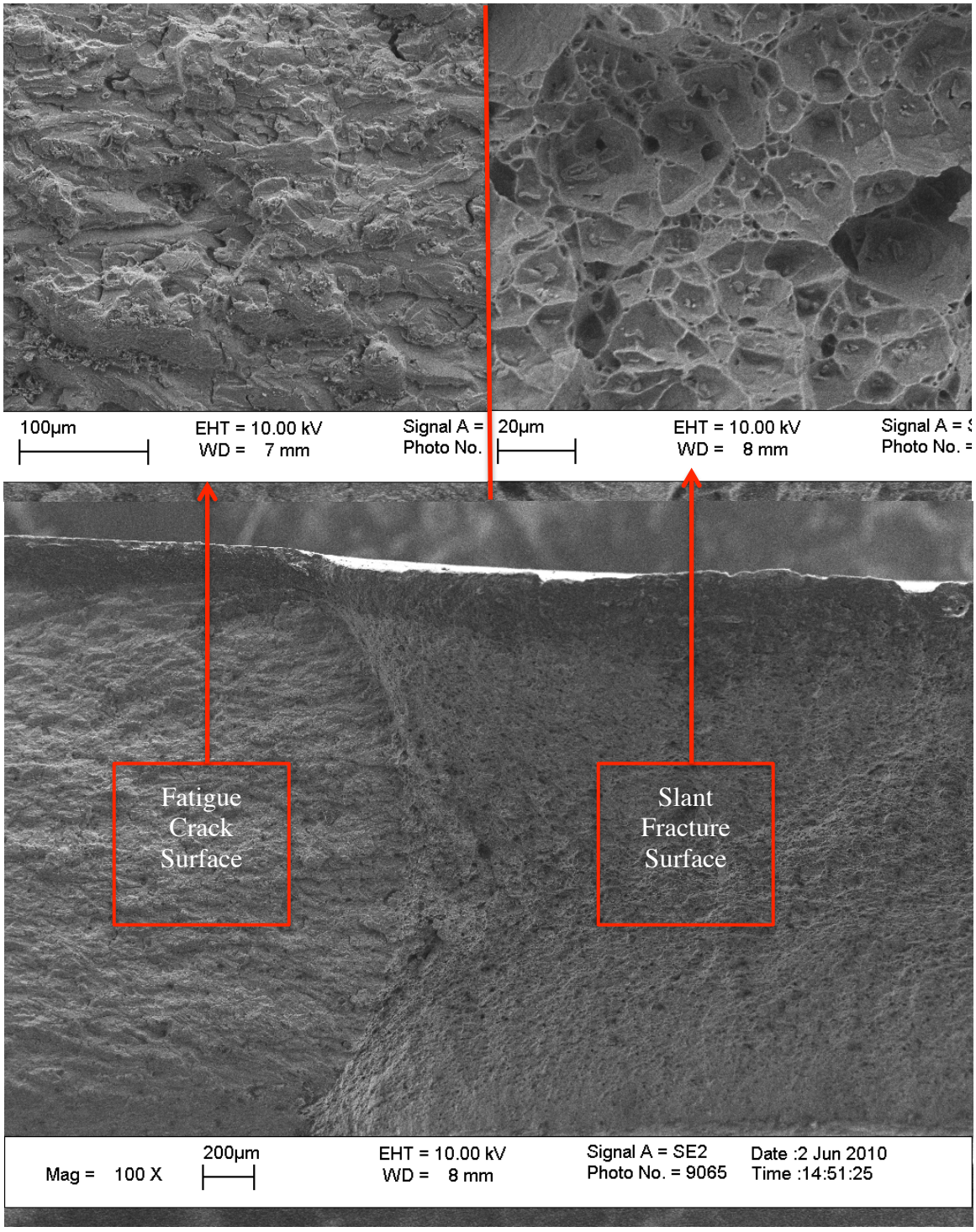

Figure 4.6: Fracture surface of Al 6061-T6

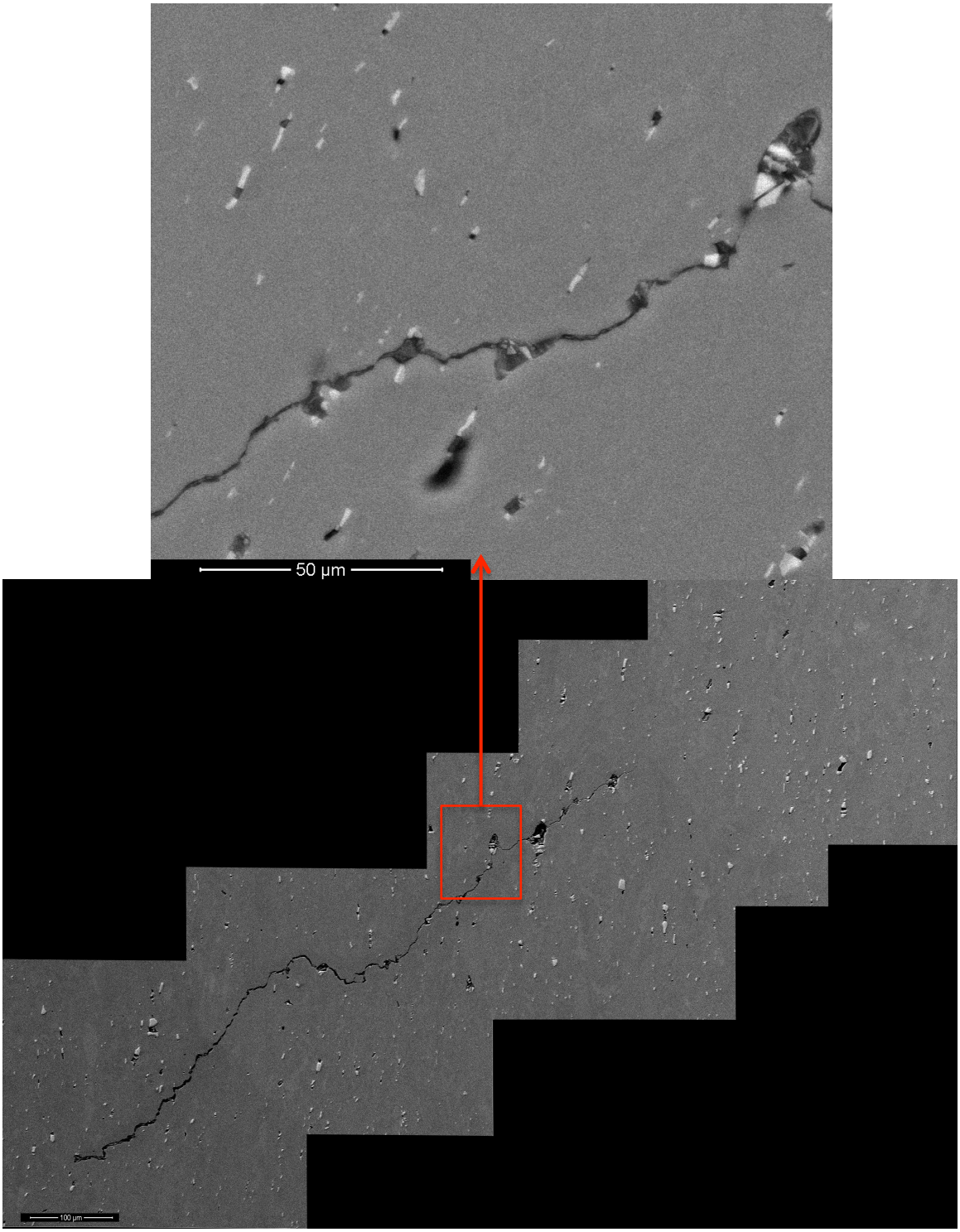

Figure 4.7: Tunneling crack in Al 6061-T6

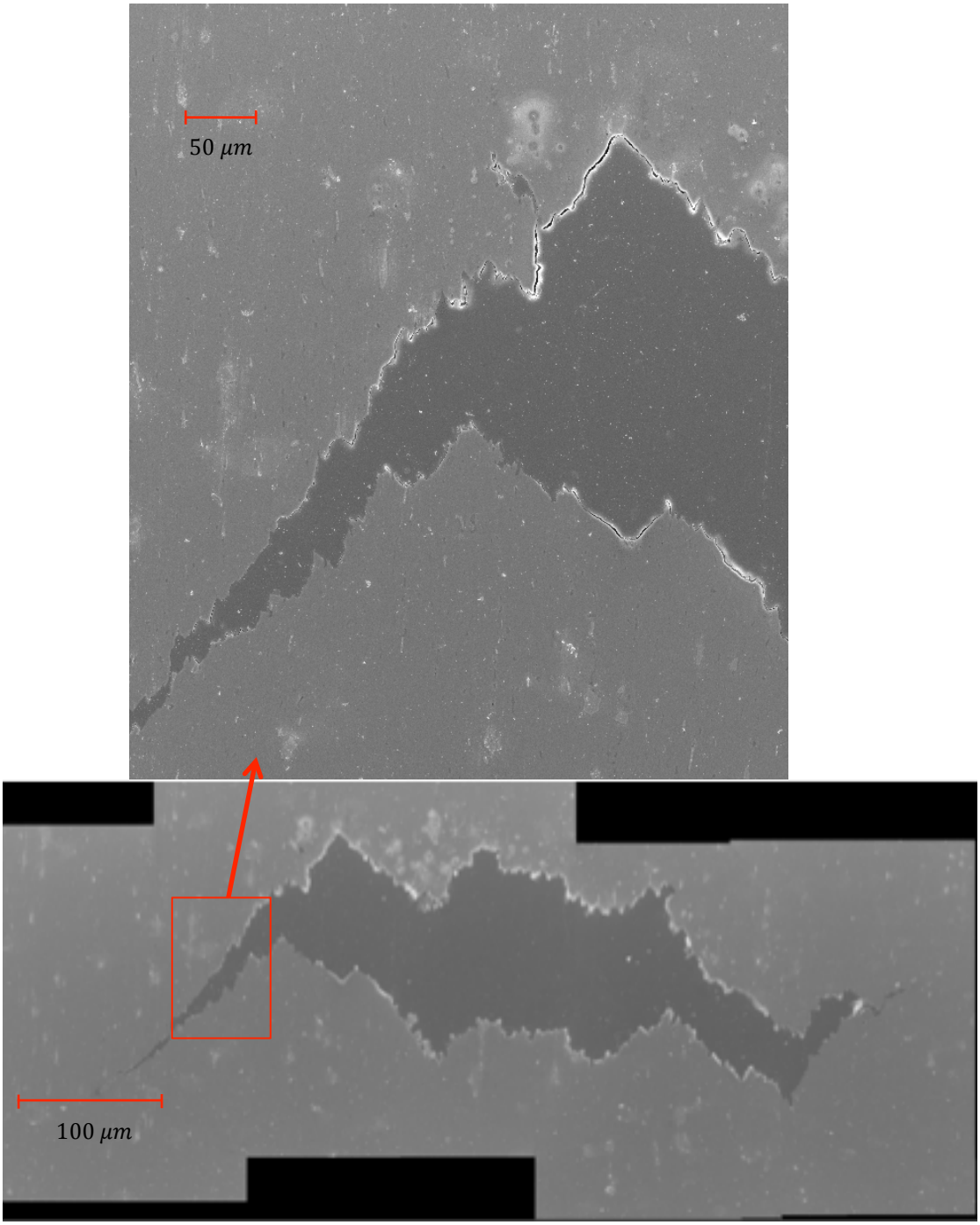

Figure 4.8: Tunneling crack in Al 6061-O

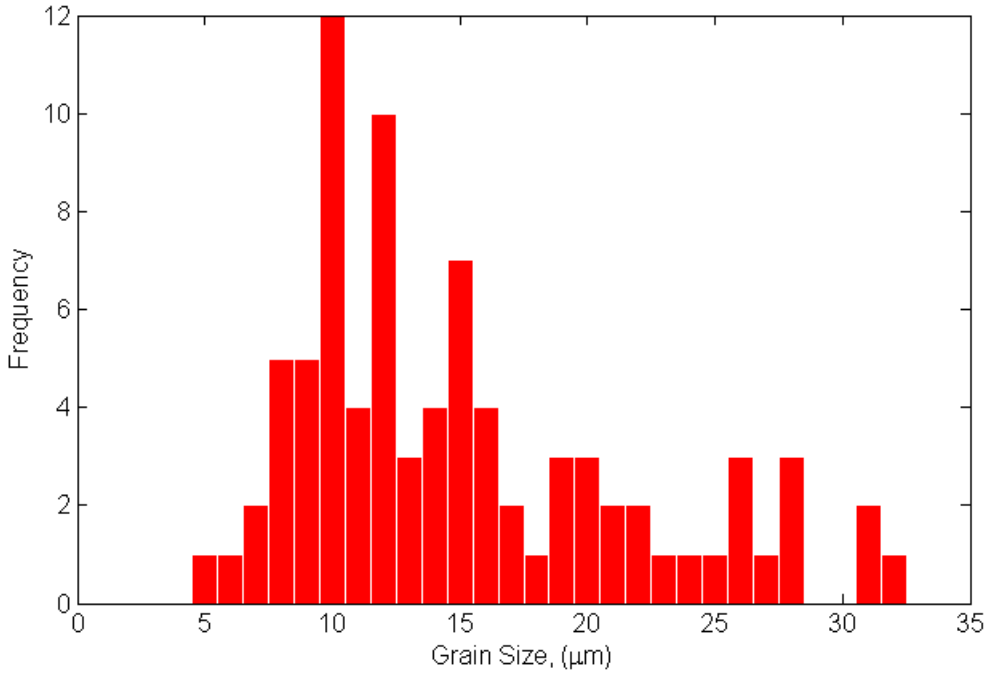

Figure 4.9: Initial grain size distribution in untested section of Al 6061-T6

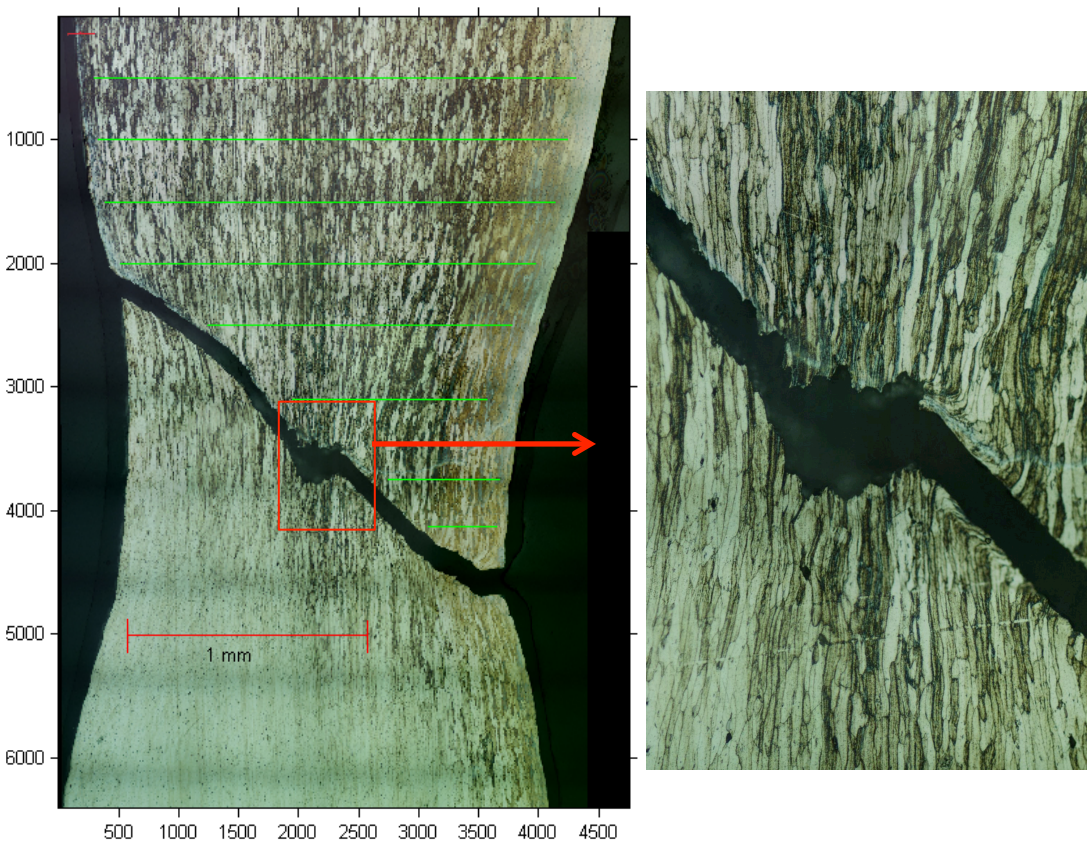

Figure 4.10: Etched Al 6061-T6 fracture specimen

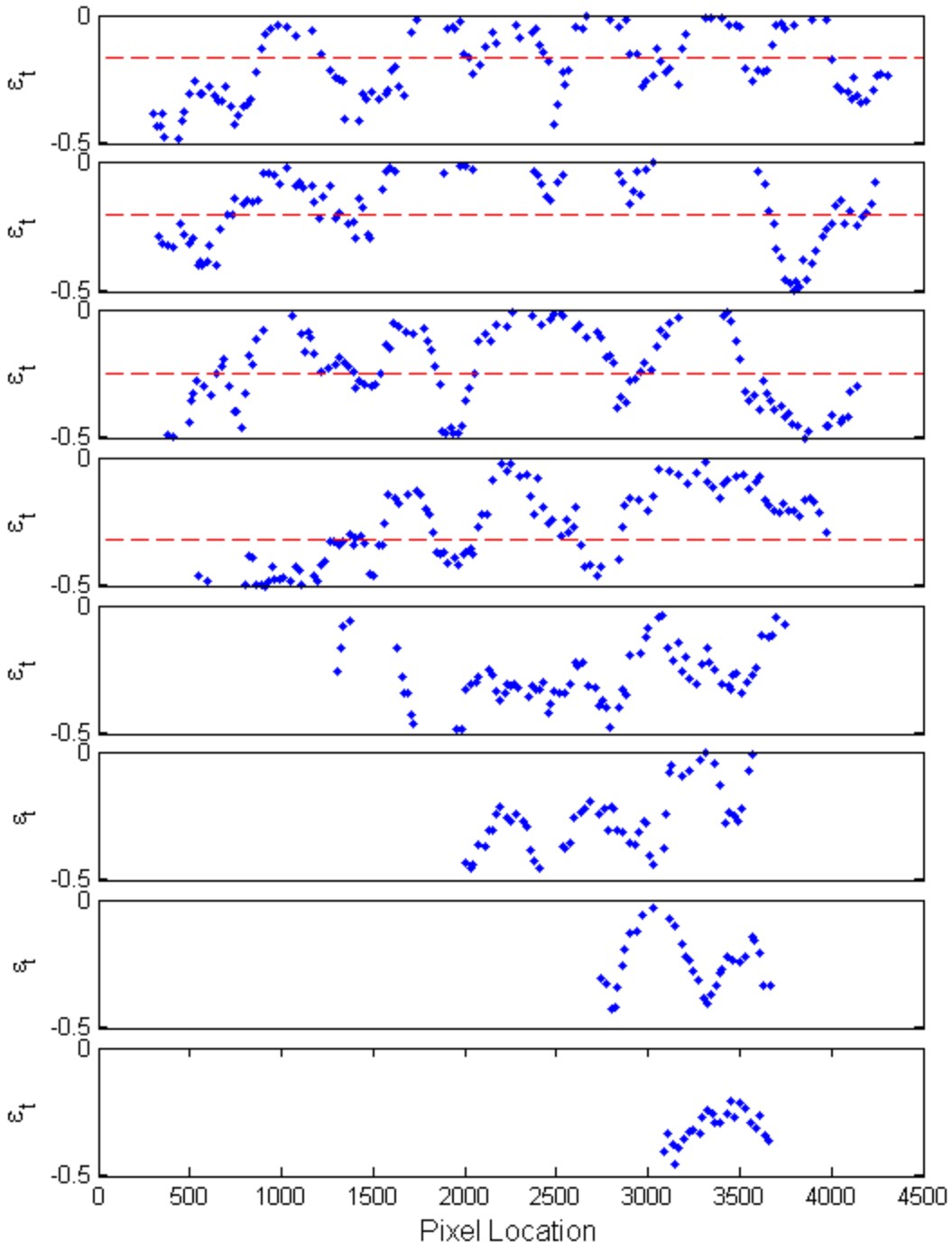

Figure 4.11: Grain level strain measurements from green lines in Figure 4.10

Chapter 5: Conclusion

Ductile failure in aluminum alloys has been characterized by first examining the data from tension tests at various strain rates for aluminum alloys in the thin sheets. Neither the Al 6061-T6 nor Al 5083-H116 exhibited any rate dependent behavior. While the macroscopically measured uniform and failure strains did increase, the stress-strain behavior did not change. For the Al 7075-T73 material, rate dependence was observed in the stress-strain response; however, the macroscopically measured strains only had modest gains.

Images of SENT plane-stress fracture tests of Al 6061 in the T6 and O conditions were recorded and analyzed using digital image correlation. With the resulting displacement and strain fields, a MATLAB routine was created to calculate the stress fields. Consequently, the J-integral was evaluated for both materials. The critical J value for Al 6061-T6 was $\sim 78\, kJ/m^2$ and $\sim 110\, kJ/m^2$ for Al 6061-O. These results are much greater than those predicted using the stress-intensity factor calculated from linear elastic fracture mechanics. The values of the J-integral from load-displacement measurements were approximated to be much higher; however, the load-train compliance and specimen geometrical effects were not properly taken into account. The J-integral results were verified by performing multiple tests. For both materials, the plots of Load vs. J-integral were identical for the additional tests. The T6 exhibited slant fracture while the O experienced flat fracture.

A large-scale test was performed on the Al 6061-T6. This specimen measured a total of 10 inches wide with an EDM notch of 5 inches. The change in crack length was recorded by post processing images, and the J-integral for steady-state crack growth was identified to be $\sim 150\, kJ/m^2$. These results were plotted with a small-scale test. During

the small-scale test, the value of the J-integral continued to increase until failure. This can be attributed to boundary conditions; as the load increased and the crack moved further from the load line, the specimen began to rotate in the grips and thus distorting the J-integral values.

The HRR fields were calculated and contours of equivalent stress were plotted and compared with the experimental results of the small-scale tests. These results confirmed that the HRR equations do not properly capture the slant fracture localization and the equivalent stress is overestimated in the both the T6 and O materials; however, the HRR equations do capture the general shape of the flat fracture localization.

Comparing the major strain fields highlighted differences in the localizations of the two materials. Both materials are in a state of plane stress, and the difference in the localization is attributed to the strain hardening behavior of each material. Because of the low strain hardening of the T6 material, the localization occurs ahead of the crack tip very early, and the plastic zone does not fully develop. The localization does not deviate from the $\pm 45°$ planes, and fracture occurs here. On the contrary, the annealed material exhibits significant strain hardening, and the localization that develops does not do so until the material is significantly strained. This allows for thinning in the sheet and a region of high triaxiality to exist in front of the crack tip which in turn causes classical ductile fracture perpendicular to the loading direction.

The fracture surfaces of both materials were examined using optical and scanning electron microscopy. The fatigue crack regions were observed to be flat for both materials, and the fracture surfaces showed failure by void growth and coalescence.

The fracture specimens were further dissected and mounted into epoxy. After proper polishing, the specimens were etched to reveal the grain structure. Measurements of grain level strains were completed and compared with the macroscopic level strains.

Grains very close to the fracture surface were measured to determine a microscopically measured failure strain. For Al 6061-T6, the grain level failure strain was 0.67, while the macroscopic estimate of failure strain was 0.51. In the Al 6061-O material, the grain level failure strain was measured to be 1.06, and the macroscopically measured strain was 0.75. These large increases in the failure strains indicate that the failure occurs in an extremely localized region. This has further implications for modeling of fracture and failure. Common techniques used today do not properly capture this failure strain due to the influence of mesh size on the result. The nature of these localized failures implies that the mesh size must be sufficiently small to properly account for the failure strains.

Bibliography

Bao, Y., Wierzbicki, T., 2004, On fracture locus in the equivalent strain stress triaxiality space, International Journal of Mechanical Sciences, 46, 81-98.

Bruck, H.A., Chae, T.L., Chao, Y.J., Sutton, M.A., Turner, J.L., 1992, Experimental investigations of three dimensional effects near a crack tip using computer vision, International Journal of Fracture, 53, 201-228.

Chu, TC, Ranson, WF, Sutton, MA, Peters, WH, 1985, "Applications of Digital-Image Correlation Techniques to Experimental Mechanics," Experimental Mechanics, 25, 232-244.

Kanninen, Melvin F. and Poplar, Carl H., 1985, Advanced Fracture Mechanics. New York: Oxford University Press.

Kant, Yi-Lan, Qin, Qing-Hua, Wang, Huai-Wen, 2005, Experimental investigations of the effect of thickness on fracture toughness of metallic foils, Materials Science and Engineering A, 394, 312-319.

Kaufman, J. Gilbert, 2000, Introduction to Aluminum Alloys and Tempers. 1st ed.: ASM International.

Leistner, E. and Weck, E., 1986, Metallographische Anleitung zum Farbatzen nach dem Tauchverfahren, Part III, DVS Dusseldorf.

Li, F.Z., Shih, C.F., Needleman, A., 1985, A comparison of methods for calculating energy release rates, Engineering Fracture Mechanics, 21, 405-421.

MacKenzie, D. Scott and Totten, George E., 2003, Handbook of Aluminum: Volume 2: Alloy Production and Materials Manufacturing. CRC Press.

Matlab User's Manual, Version R2009a, Mathworks Corporation, 2009.

Owen, D.M., Ravichandran, G., Rosakis, A.J., Zhuang, S., 1998, Experimental determination of dynamic crack initiation and propagation fracture toughness in thin aluminum sheets, International Journal of Fracture, 90, 153-174.

Rice, J.R., 1968, A path independent integral and the approximate analysis of strain concentration by notches and cracks, Journal of Applied Mechanics, 35, 379-386.

Zehnder, Alan T., 2007, Lecture Notes on Fracture Mechanics.